

MODELLING INTERSTELLAR EXTINCTION IN STELLAR POPULATIONS

Alexander Lisboa-Wright

A thesis submitted in partial fulfilment of the requirements of Liverpool John Moores
University for the degree of Master of Philosophy

Astrophysics Research Institute
Faculty of Engineering and Technology

July 2019

Abstract

In stellar astrophysics, the determination of the magnitude of interstellar extinction is critical, due to its effect on the observed brightness and colour of the stars. Extinction is therefore an important factor in deriving scientific information from the colour-magnitude diagrams (CMDs) of stellar populations. The treatment of extinction in standard CMD analyses is to employ constant ratios of extinction in each photometric filter relative to the visual Johnson- V filter, denoted A_X/A_V in a generic filter X .

This work presents a theoretical analysis of the behaviour of the extinction ratio A_X/A_V in multiple photometric systems as the values of three stellar parameters (effective temperature, surface gravity and metallicity) were varied. The results of this analysis show significant variations in the value of A_X/A_V with changes in the stellar parameters. Analytic functions of these stellar parameters are proposed to describe these variations.

Also presented is an application of these results to a highly-reddened star cluster whose members also have accurate Gaia parallax measurements. When a proper analysis, which considers the variation of extinction ratios with stellar parameters, is used on the cluster data, it is shown that there is a non-negligible impact on the age determination for the cluster.

Units & Terminology

Unless stated otherwise, all quantities will be described in CGS units (masses in grams, lengths in centimetres, times in seconds, energies in ergs).

In this project, the notation $\log(x)$ represents the logarithm of x to the base 10. The natural logarithm of x will be expressed as $\ln(x)$.

Each of the quantities below is relevant to this project and, unless stated otherwise, will be the only quantity denoted by the symbol assigned to it below.

M : mass

Luminosity : L

Radius : R

Gravitational acceleration : g

Solar mass : $M_{\odot} = 1.989 \times 10^{33} \text{ g}$

Solar luminosity : $L_{\odot} = 3.842 \times 10^{33} \text{ erg s}^{-1}$

Solar radius : $R_{\odot} = 6.957 \times 10^{10} \text{ cm}$

Gravitational constant : $G = 6.6723 \times 10^{-8} \text{ cm}^3 \text{ g}^{-1} \text{ s}^{-2}$

Stefan-Boltzmann constant : $\sigma_{\text{SB}} = 5.678 \times 10^{-5} \text{ erg cm}^{-2} \text{ K}^{-4} \text{ s}^{-1}$

parsec (pc) : $1 \text{ pc} = 3.086 \times 10^{18} \text{ cm}$

Chapter 1

Introduction

1.1 Interstellar extinction

1.1.1 Physical origin & definition

As the light emitted from a star travels towards a distant observer, its intensity, or flux decreases with distance via an inverse-square law. Stars emit light across the full range of electromagnetic spectrum. Therefore, a beam of light from a star will consist of photons with an extremely wide range of wavelengths.

However, the interstellar medium (ISM) is not a perfect vacuum. It contains many different structures, such as clouds of diffuse gas and dust grains, that can absorb or scatter light passing through. For a given light source, this causes its brightness to appear lower than it would otherwise and changes the distribution of the same brightness with photon wavelength. The effect of dust clouds on optical light travelling towards observers is particularly apparent when examining star clusters and galaxies (including the Milky Way), with the dust obscuring optical light from sources behind the clouds.

Interstellar extinction is defined physically as the magnitude of the flux absorbed or scattered by the intervening line-of-sight ISM. Mathematically, extinction, A , is defined using the standard astronomical system of flux magnitudes via the following equation:

$$m - M = 5 \log \left(\frac{d}{\text{pc}} \right) - 5 + A \quad (1.1)$$

where m is the apparent magnitude of the source, M is its absolute magnitude and d is the distance to the source.

When a broadband beam of light passes through a cloud, the loss of flux due to absorption, refraction or diffraction is related to the optical depth, τ . The optical depth is defined along the line-of-sight via:

$$\tau(l) = \int_0^l \rho \kappa dl = \int_0^l n \sigma dl \quad (1.2)$$

where l is the length of the path taken by the beam through the cloud, ρ is the mass density of the local cloud material, κ is the material's opacity, n is the particle number density and σ is the particle collision cross-section.

It should be noted that all quantities in the integrands in Equation 1.2 depend on local conditions at each point in the path travelled by the beam. In particular, the opacity, for a given wavelength, depends strongly on the available configurations for the atomic electrons in the cloud, which in turn depend on the chemical composition of the cloud. Although the light absorbed by atomic electrons is re-radiated, for a large number of electrons this radiation is emitted isotropically, causing a net decrease in the flux travelling in the direction of a given observer.

The quantities in Equation 1.2 therefore cannot be immediately discounted as being constant along the entire path required for the integration, let alone throughout the entire cloud. Furthermore, the dependence of opacity, and subsequently optical depth, on the composition of the medium causes a variation of its value with the wavelength of photons in the beam. This necessitates the specification of the optical depth being applicable for X in Equation 1.2.

The variation in flux of the light beam with distance travelled through the cloud is best expressed using the optical depth:

$$f = f_0 e^{-\tau} \quad (1.3)$$

where f is the flux of the beam after it exits the cloud and f_0 is the flux at the point where the beam first encounters the cloud (i.e., at $l = 0$). Returning to the equation for flux magnitudes given in Equation ??, we can use the relation in Equation 1.5 to rewrite Equation ?? as:

$$A = m - m_0 = -2.5 \log \left(\frac{f}{f_0} \right) = -2.5 \log(e^{-\tau}) \quad (1.4)$$

Therefore, we can define the extinction in terms of the distance travelled through, and the composition of, the ISM, both of which are accounted for in the optical depth:

$$A = 2.5 \log(e) \times \tau = 1.086 \tau \approx \tau \quad (1.5)$$

In conclusion, to a first-order approximation, the extinction is equal to the optical depth along the line of sight. Hence, the mathematical representation of extinction is proven to be aligned with its physical definition as the flux of photons scattered and absorbed in the interstellar medium.

The incidence of absorption and scattering events depends on the wavelength of the incoming photons. This dependence is also incorporated into the optical depth via the scattering cross-section σ in Equation 1.2. If the particles in the ISM are (naively) assumed to be spherical with radius a , its geometric cross-section is πa^2 for any incoming photon. Using the scattering and geometric cross-sections, a dimensionless extinction coefficient:

$$Q(\lambda) = \frac{\sigma(\lambda)}{\pi a^2} \quad (1.6)$$

can be defined. When the photon wavelength is on the order of the particle size ($\lambda \sim a$), Mie (1908) showed that $Q \sim a/\lambda$. In the limit $\lambda \gg a$, Q decreases to zero, while for $\lambda \ll a$, Q becomes constant with regard to wavelength. This shows that, for extinction in the UV-to-near-IR spectral range, which covers approximately a 100-1000 nm wavelength range, the scattering cross-section for relevant ISM atomic species is proportional to $1/\lambda$. Typical interstellar dust grains have radii (a) ranging between 100 and 1000 nm (Witt, 2000), but the dominant grain size is 300 nm (Landgraf et al., 2003). Therefore, Q is greatest when the photon wavelength is in the region of 300 nm, which is located within the UV regime. The effect of extinction, is therefore significantly greater in the UV than in the IR. Although, as mentioned previously, this model is overly simplistic, its general conclusions align with observational results. Therefore, referring back to Equation 1.5, interstellar extinction is also greater at shorter wavelengths, causing the source star to appear redder than its true colour (see Section 1.3). Hence, the effect of extinction is sometimes referred to as “reddening”.

A beam containing photons with a sufficiently large range of wavelengths will therefore lose some of its photons, and therefore flux, due to interactions with the ISM through which it travels. The magnitude of loss is determined by the wavelength(s) of those photons, the fraction of the beam consisting of these photons and the state of the ISM. For a given source, its interstellar extinction value represents the total flux absorbed or scattered due to all extinction events along the line-of-sight between the source and the observer.

1.1.2 Empirical extinction curves

The variation of extinction with wavelength discussed in the previous section has been studied for decades. Various authors have produced empirical results intended to better model the changes in the magnitude of extinction over an extended wavelength range, as explicit functions of wavelength or as values or functions unique to each in a selection of photometric filters.

Rieke & Lebofsky (1985) found that outside dense molecular clouds, which have high opacities and whose lines-of-sight are less frequently used as a result, all extinction

laws for all Johnson filters studied were uniform between wavelengths of 1 and 13 μm when observing sources in the direction of the Galactic Centre. This result was then used to produce constant A_X/A_V extinction ratios in the same filters. They also determined the now-widely used global average value of 3.08 (3.1) for $R_V = A_V/E(B-V)$, known as the total-to-selective extinction ratio, for the diffuse ISM.

Cardelli et al. (1989) used observations of mostly O- and B-type main-sequence stars to produce empirical equations describing the mean ratio of extinction values at a specific wavelength λ (A_λ) to the extinction in the Johnson- V filter (A_V), respectively. From this point onward, this ratio will be referred to as A_λ/A_V . They produced a basic equation of the form:

$$A_\lambda/A_V = a(x) + b(x)/R_V, \quad (1.7)$$

where $x \equiv 1/\lambda$ and $R_V \equiv A(V)/E(B-V)$. The significance of R_V , as noted in the same paper, comes from its usefulness as an indicator of the nature of the interstellar medium through which the observed light travels in order to reach the observer. The total wavelength range was divided into 4 sub-ranges, each with a governing pair of empirically-determined equations to calculate $a(x)$ and $b(x)$, respectively. The resulting extinction-ratio profiles for three lines of sight are displayed in Figure 1.1. This model underpins more recent studies of intrinsic effects on extinction (Girardi et al., 2008; Casagrande & Vandenberg, 2018), and provides the basis for the synthetic A_X/A_V datasets in this project. Equation 1.7 has become a standard model for theoretical studies to employ for predictions made in the UV, optical and near-IR wavelength regions, although it is not always accurate (O'Donnell, 1994; Fitzpatrick, 1999).

O'Donnell (1994) found deviations from the Rieke & Lebofsky (1985) extinction law in the soft-UV spectral range using a sub-sample of 22 stars from the same dataset. This was attributed to the uncertainty in the short-wavelength cutoff of the UV-range Johnson U filter and to the presence of the Balmer discontinuity within the limits of the filter bandpass.

Fitzpatrick (1999) found that, due to the broadband nature of the Johnson filters and the general decrease of extinction with wavelength, the Cardelli et al. (1989) relations overestimate the extinction in the near-IR and blue-visible Johnson filters. The study put forward corrections to the equations for $a(x)$ and $b(x)$ for these wavelength regions. However, in the UV region covered by the Cardelli et al. (1989) equations, the equations are accurate for 93% of a homogeneous UV observational database (Valencic et al., 2004).

Girardi et al. (2008) produced data tables of A_X/A_V for stellar atmosphere models with parameters T_{eff} , $\log(g)$ and $[\text{Fe}/\text{H}]$. They carried this out using the same ATLAS9 data (Castelli & Kurucz, 2004) that was used to generate the data for this project, but also combined it with data from other studies Girardi et al. (2002), resulting in

data covering a parameter space extending beyond the ATLAS9 limits in all three parameters. They used the data tables to calculate the A_X/A_V values for the stellar models in Padova theoretical isochrones. While determining that the values of A_X/A_V varied significantly with T_{eff} and $\log(g)$, the variation with metallicity was found to be 0.17% between $[\text{Fe}/\text{H}] = 0.0$ and $[\text{Fe}/\text{H}] = -2.5$. They found that, when they set $A_V = 6$, there was a systematic shift for the ACS system between extinction values calculated star-wise using the tables of A_X/A_V data and a constant extinction value. The constant values of A_X/A_V were calculated from a yellow dwarf in the low-extinction regime. Overall, the A_X/A_V tables produced a smaller extinction value in the F814W filter and a larger (F475W-F814W) colour index value. It also caused a change in the shape of the curve at the MSTO. They then applied the data from the tables to the case of the globular cluster M92. They found the optimal metallicity to be $Z = 0.0004$ ($[\text{Fe}/\text{H}] \approx -1.6$) instead of the value obtain by previous observers of $Z = 0.0001$ ($[\text{Fe}/\text{H}] \approx -2.2$). Therefore, their use of A_X/A_V data caused the estimated cluster metallicity to be greater than when using the standard one-size-fits-all approach to extinction.

Casagrande & Vandenberg (2014, 2018a, 2018b) created simple models for the parameter $R_X = \frac{A_X}{E(B-V)}$, consisting of a quadratic variation with effective temperature and a linear variation with metallicity (they found no significant variations with surface gravity) in multiple telescope filter systems. This was based on MARCS model stellar atmospheres, which have an upper T_{eff} limit of 8000K (Gustafsson et al., 2008). The equation is independent of surface gravity and has the following form:

$$R_X = a_0 + T_4(a_1 + a_2 T_4) + a_3 [\text{Fe}/\text{H}] \quad (1.8)$$

where $T_4 = 10^{-4} \times T_{\text{eff}}$. The equation is valid for $5250\text{K} \leq T_{\text{eff}} \leq 7000\text{K}$. Although these models are mathematically simple (with only 4 coefficients), the limited T_{eff} range in which they are applicable is problematic, particularly in the red giant branch (RGB) and lower main sequence of any stellar population.

1.2 Extinction in stars & stellar populations

1.2.1 The effect of extinction on the observed magnitudes of different stellar types

This project examines the effect of extinction treatment methods on interpretations of observed stellar populations. To understand how extinction affects the observed magnitudes of different stellar types, we must first define the fundamental parameters that describe a stellar atmosphere, which will be used in this project as the input variables on which any star-to-star variations in extinction will be modelled.

The effective temperature (T_{eff}) of a star is defined as the thermodynamic temperature of a black body which produces the same stellar flux across all wavelengths (known as the bolometric flux) as that produced by the star. The equation of the radiation emitted by a black body produces the body's flux per unit wavelength per unit angular viewing area, $F_{\lambda,bb}$, known as the black body's monochromatic flux. The equation, known as the Planck Law, is as follows:

$$F_{\lambda,bb} = \frac{2hc^2}{\lambda^5 \left(\exp \left(\frac{hc}{\lambda k_B T} \right) - 1 \right)} \quad (1.9)$$

where T is the thermodynamic temperature of the black body, h is Planck's constant, c is the vacuum speed of light and k_B is Boltzmann's constant. This equation also holds if the light wave frequency is used instead of the wavelength, with the monochromatic flux $F_{\nu,bb}$ now being the black body flux per unit frequency:

$$F_{\nu,bb} = \frac{2h\nu^3}{c^2 \left(\exp \left(\frac{h\nu}{k_B T} \right) - 1 \right)} \quad (1.10)$$

In this project, the definition of monochromatic flux for any given object will be reserved exclusively for the flux per unit wavelength, F_{λ} , with any calculations involving black body fluxes using Equation 1.9.

The general approximation of stars to black bodies (and hence the actual stellar surface temperature to T_{eff}) is valid because all stars have been observed to have spectra that closely resemble those of black bodies, with the notable exception of atmospheric absorption lines. The (intrinsic) luminosity of a star is used to define the effective temperature via:

$$L = 4\pi R^2 \sigma_{SB} T_{\text{eff}}^4 \quad (1.11)$$

where R is the (mean) stellar radius. Effective temperature has an effect on interstellar extinction due to its strong effect on the stellar luminosity and, hence, the flux, via the Planck Law in Equation 1.9. For a higher effective temperature, there will be more photons in the broad beam of light with wavelengths that make them likely to interact with the local ISM.

Different chemical elements have different orbital configurations of atomic/ionic electron states. Each electron state absorbs and emits photons at a particular wavelength, which varies between individual states and between elements. Therefore, a greater proportion of light in a broadband beam is absorbed in a medium containing a mixture of many different elements than in a medium dominated by one or two elements. From astrophysical observations, it is clear that hydrogen is by far the most abundant element in the universe, with helium a clear-but-distant second. The metallicity of a star is defined as the fractional abundance of heavy elements, often approx-

imated by iron (Fe) alone, relative to the star’s hydrogen (H) abundance, compared to that of the Sun. The abundances are determined by the strength of the elements’ characteristic atomic absorption lines in the stellar spectra.

$$[\text{Fe}/\text{H}] = \log \left(\frac{N_{\text{Fe}}}{N_{\text{H}}} \right) - \log \left(\frac{N_{\text{Fe},\odot}}{N_{\text{H},\odot}} \right) \quad (1.12)$$

For a generic atomic species E , N_E represents its number density. For stellar observations, N_E is measured at the surface. Since the output is logarithmic, a value of $[\text{Fe}/\text{H}] = 0$ indicates solar metallicity. An increase in metallicity would cause the corresponding absorption lines to be stronger, thus reducing the observable flux. An increased metallicity also implies an increase in abundance of sub-ferrous metals. The presence of more nuclear species, each with unique absorption line configurations, inevitably creates more observable lines, further increasing the apparent extinction in the spectral flux. The effect of this reduction in flux manifests itself as a reduction in the stellar luminosity and therefore the effective temperature when all other stellar properties (such as the mass and age) are fixed. The position of the star

The definition of the stellar surface gravity g is simply the value of the standard Newtonian gravitational acceleration, applied to the stellar surface (the mass is the total stellar mass, M_* , and the distance is the stellar radius, R_*):

$$g = \frac{GM_*}{R_*^2} \quad (1.13)$$

A greater surface gravity, as can be inferred from Equation 1.13, represents a surface with a higher mass density. For stars, being self-gravitating, this infers a higher atomic number density.

The effects of surface gravity on the stellar emission spectrum arise directly from the quantum properties of the interactions between the photons and atomic electrons in the stellar atmosphere.

When a particle, such as an electron, absorbs a photon, the absorption process is not instantaneous and therefore carries an uncertainty in the time taken for the process to be completed, with a corresponding uncertainty in energy due to the Heisenberg uncertainty principle. Across a large number of absorptions for the same initial electron state, the result is a spread in the energies of the absorbed photons. The associated emission line is therefore broadened by the multiple wavelengths of the photons. This is universal and referred to as “natural broadening”.

The impact of surface gravity arises via additional broadening effects upon these same absorption lines. When broadening effects are applied to an emission spectrum, such as a spectrum from a stellar surface, the result is that fewer photons pass through the surface, thereby reducing the surface flux seen by an outside observer.

The impact of stellar effective temperature, metallicity and surface gravity on extinction arises through their described effect on the spectral energy distribution (SED) emitted by the stellar atmosphere. Since both the SED and the magnitude of the interstellar extinction are functions of wavelength, different stellar types, with different SEDs, can be impacted to different extents by interstellar extinction at a given wavelength.

1.2.2 Forbes effect

The Forbes effect occurs as a broadband beam of light, such as that passes through an extended partially-transparent medium, such as the Earth's atmosphere or an interstellar gas or dust cloud. It states that the greater the distance travelled by a light beam through the medium, the more penetrating the beam becomes (Forbes, 1842). The physical basis for this effect is that those photons in the original beam with wavelengths that make them the most likely to be absorbed or refracted are separated from the beam earlier. Therefore, as the beam travels through the medium, its constituent photons are progressively less likely to be interact with the medium (Grebel & Roberts, 1995). Since a higher fraction of its photons are retained as the distance through the medium increases, the beam is more penetrating (Ohvri et al., 1999).

This has the effect of producing a non-linear increase in extinction for one filter relative to the increase in another (Grebel & Roberts, 1995; Girardi et al., 2008). It should be emphasised that the Forbes effect occurs regardless of the source star's spectral type, and therefore represents an additional source of uncertainty when calculating extinction for highly-reddened stellar populations.

1.2.3 Determining properties of stellar populations

The role of CMDs

If we compare the individual black body spectra in Figure 1.2, it can be seen that the maximum monochromatic flux of the black body occurs at an increasingly shorter wavelength for objects with increasingly higher temperatures. This makes the object appear bluer to an observer. The relationship between the wavelength at which the monochromatic flux is maximal (λ_{max}) and the black body temperature is quantified by Wien's displacement law:

$$\lambda_{max}T = 2.898 \times 10^6 \text{ nm K} \quad (1.14)$$

More importantly, Figure 1.2 demonstrates that, within the UV-to-IR wavelength regime, the change in monochromatic flux between values at two different wavelengths is always greater for stars with higher effective temperatures. Therefore, to measure

a star's effective temperature, observers compare the star's observed flux in two filters operating at different wavelengths within this range. The difference between the star's flux magnitudes in each of the two filters is then taken, with the flux in the redder filter being deducted from that of the bluer filter. This quantity is known as the colour index. For two filters X and Y , with X being bluer than Y , the colour index of observations made using those filters, $(X - Y)$, is defined as:

$$\begin{aligned}(X - Y) &= m_X - m_Y \\ &= (m_{X,0} - m_{Y,0}) + (A_X - A_Y) \\ &= (X - Y)_0 + E(X - Y)\end{aligned}\tag{1.15}$$

where $(X - Y)_0$ is the true or intrinsic colour index of the object and $E(X - Y) = A_X - A_Y$ is known as the colour excess, but can also be denoted in literature using the term “reddening”. The colour excess represents the effect of extinction on the observed colour index. Its importance arises from the prominence of the intrinsic colour index in determining effective temperature. Higher values of $(X - Y)$ indicate redder stars, with lower effective temperatures.

The most commonly-used colour index, employed as a reference for most optical observations, is the Johnson $(B - V)$ index (Johnson & Morgan, 1953). This is due to these filters being the among most widely-used and best-studied available, allowing for better comparisons of different data, including data from older archives.

It can be seen from Equation 1.11 that the luminosity (and therefore flux) of a star is dependent on radius as well as effective temperature. If a plot is made of luminosity against effective temperature (a Hertzsprung-Russell diagram), it can be seen that all stars in a given star cluster follow a single, complex track. Because the stars are approximately the same age in a typical cluster population, this track is known as an isochrone. Isochrones for different population ages and metallicities are calculated using theoretical stellar models, which cover the largest possible spread of initial stellar masses for the required age.

By examining the flux-magnitude equations from both this section and Section 1.1, it becomes clear that both the absolute filter magnitudes and the intrinsic colour indices can be used, together with bolometric corrections, to calculate the luminosity from observational data. To determine the detailed properties of stellar populations, all stars in an observational sample or star cluster are plotted together on a pair of axes known as a colour-magnitude diagram (CMD), which represents an observational analogue of the HR diagram. The absolute magnitude of stars in a given filter Z , M_Z , is on the y-axis, with the flux increasing (and the magnitude value decreasing) upwards. The intrinsic colour index of the stars in two filters X and Y , $(X - Y)_0$, is on the x-axis, with the values increasing (and stars becoming redder) to the right. In practice, due to the unknown extinction values for the individual stars and the cluster

as a whole, the axial parameters are $M_{\text{ext},Z}$ and $(X - Y)$. Note that filter Z may be the same as either X or Y .

In practice, the universal general shape and position of stellar populations in the HR diagram and each observational CMD, particularly the position and shape of the main sequence, provides a highly useful tool for comparing stellar populations with unknown distances and extinction values to known examples and to theoretical models. This is done by alignment of the respective main sequences in CMDs, particularly the upper main sequence, which contains the most luminous MS stars and is less sensitive to the (initially unknown) value of the cluster metallicity than the lower MS.

The age of an observed stellar population are determined by, firstly, correcting the data for the effects of distance and extinction and, secondly, aligning a series of isochrones, each of a different age, with the main-sequence (MS) of the observed data. The accepted age of the population is that of the isochrone which most closely follows the progression of stars along the main-sequence turn-off (MSTO). As such, any errors in the estimated extinction can potentially change the age of the best-fit isochrone and therefore produce an erroneous estimate of the true population age.

Comparing theoretical and observational quantities

For any observational dataset of stars, the stars' individual extinction values will be completely unknown from the data alone. In order to compare observational and theoretical data, the most convenient approach is to add the (theoretical) extinction value(s) to the theoretical dataset magnitudes (i.e., absolute magnitudes), before comparing to the distance-corrected observational data. As a result, the quantity from each dataset that is being compared is the absolute magnitude plus the extinction in each filter. If we label this quantity $M_{\text{ext},X}$ for a generic filter X , we can define it as:

$$M_{\text{ext},X} = M_X + A_X \quad (1.16)$$

Using Equations ?? and ??, Equation 1.16 can now be rewritten such that $M_{\text{ext},X}$ is defined using both quantities derived directly from observations and those determined by theoretical models:

$$\begin{aligned} M_{\text{ext},X} &= M_X + A_X \text{ (theoretical data)} \\ &= m_X + 5 - 5 \log \left(\frac{d}{\text{pc}} \right) \text{ (observational data)} \end{aligned} \quad (1.17)$$

This allows for direct comparison of theoretical data, whose stars are treated with theoretically-determined A_X values, with distance-corrected observational data, whose stars have unknown A_X values. Therefore, this provides a pathway for comparing the standard treatment of extinction (constant A_X/A_V ratios) with the treatment proposed

in this project (A_X/A_V varying as functions of intrinsic stellar parameters).

1.3 The standard treatment of extinction in observed stellar populations

In observations, the extinction for a given source is initially unknown. For a stellar population, observers must make use distinctive features of stellar populations that can be used as standard candles to estimate distance moduli to the population (see Equation ??).

The treatment of extinction in observational surveys is usually via a constant value for the ratio of extinction in a given filter X , denoted by A_X , divided by the extinction in the well-studied Johnson- V filter, A_V . The value used for this ratio, denoted by A_X/A_V , is often taken from Rieke & Lebofsky (1985). This approach has the significant issue of producing A_X/A_V values that do not account for variations between stellar spectra due to different physical parameter values in different stellar atmospheres when integrated over the filter's wavelength range. As shown in Figure 1.2, the monochromatic flux at a given wavelength varies greatly with effective temperature, as does the ratio between monochromatic fluxes of stars of different temperatures. This makes the notion that stars of different temperatures lose the same flux in a given filter pass-band, which is implied by the use constant extinction ratios across all stellar classes, inherently flawed. Stars with higher effective temperatures have emission spectra with much higher and (proportionally greater) fluxes at the shorter wavelengths which are most impacted by interstellar extinction. Therefore, it should be expected that hotter stars experience higher extinctions A_X for a given filter, not equal values.

Ortolani et al. (2017) used the tabulated extinction ratio tables resulting from Girardi et al. (2008), which demonstrated the significant effect of stellar parameters on the calculated extinction ratios, to search for potential discrepancies in the predicted ages of isochrones after the addition of extinction. This was performed for isochrones with real ages between 12 and 13 Gyr and employed a small selection of Johnson (B , V and I) and ACS (F606W, F775W and F814W) broadband filters. They found that, once the assumption of uniform extinction across the entire population was removed by employing the Girardi et al. (2008) data, the isochrone position in the CMD shifted such that, at $A_V = 1$, the MSTO of a 12 Gyr isochrone with individual stellar extinction values added is the same as the position of a 12.5 Gyr isochrone with the standard single extinction value added.

1.4 Project objective

The first goal of this project is to investigate the variations of the extinction ratios A_X/A_V in selected photometric filters within multiple filter systems with changes in effective temperature, surface gravity and metallicity. This will be carried out using a large library of theoretical stellar spectra covering all main stages of stellar evolution. Analytic fitting functions will be employed to model the A_X/A_V variations as a function of the stellar parameters.

The results of the fitting process will then be applied to the CMD of a representative example of a relatively high-extinction open cluster. The CMD will be fitted with two theoretical isochrones. For the first case, a constant A_X/A_V value will be applied to the entire isochrone. For the second, varying A_X/A_V will be applied, using the fitting results. The best estimates for the ages and A_V values in both cases will be compared, giving a quantitative illustration of the importance of the effect of the stellar parameters on A_X/A_V ratios used in CMD fitting.

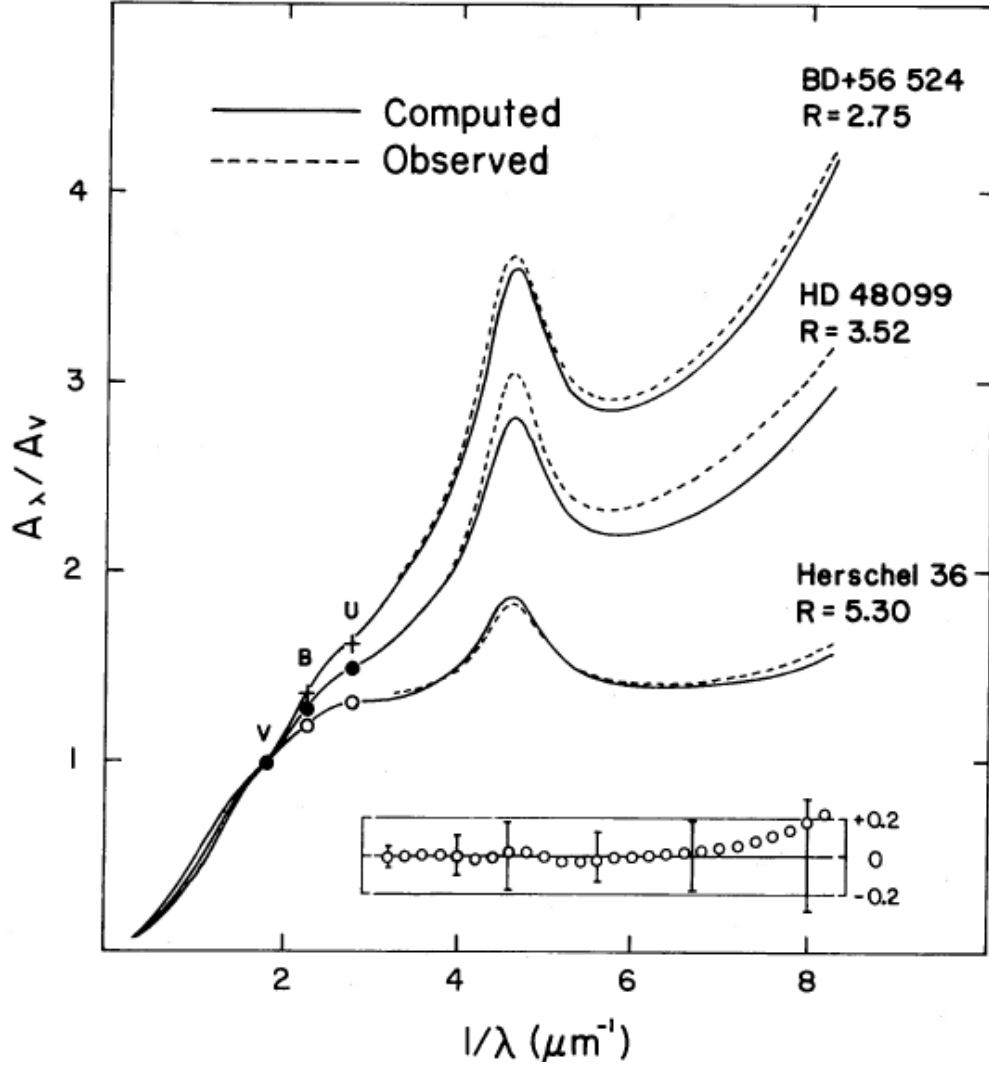


Figure 1.1: Variation of the extinction, normalised to the V-band extinction A_V , as a function of wavelength, in spectral regions ranging from the IR (left) to the UV (right). The solid lines are calculated using Equation 1.7 at the given R_V values. These values represent the lines of sight for their respective source stars, which are listed alongside. Source: Cardelli et al. (1989)

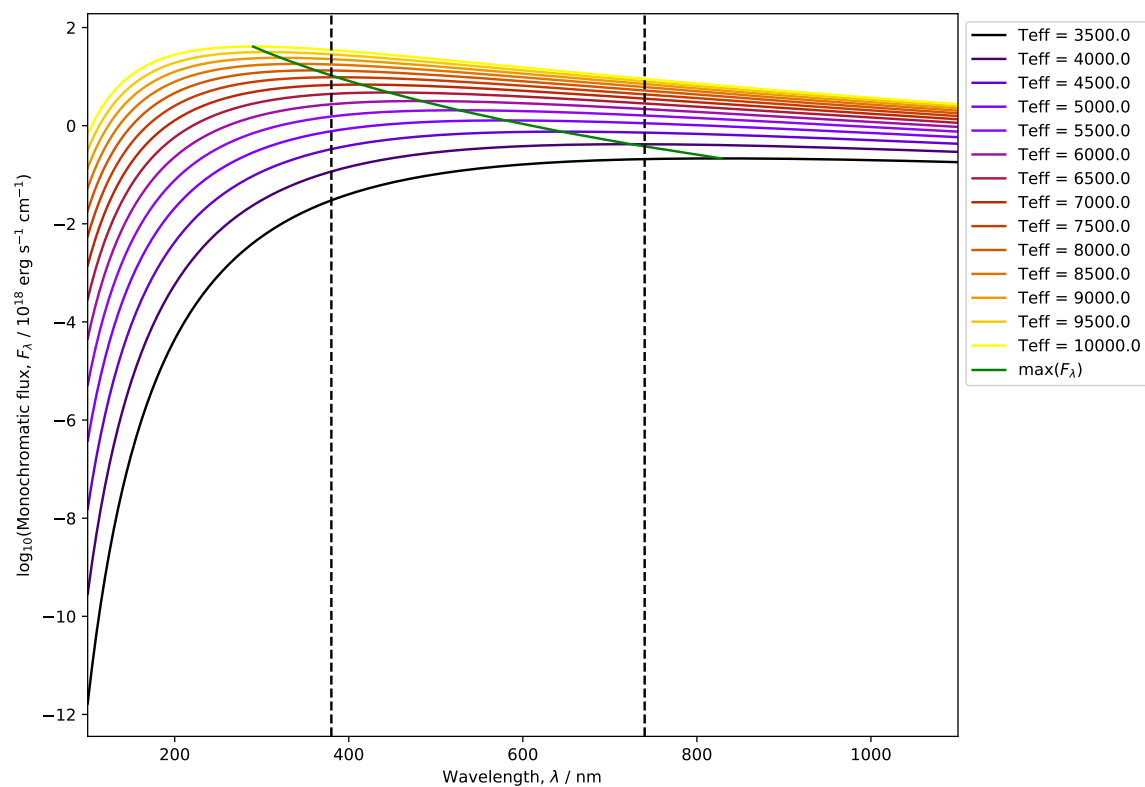


Figure 1.2: Plot of the logarithm of monochromatic flux of a black body for different stellar effective temperatures, as a function of wavelength. The black dashed lines mark the approximate limits of the visible part of the EM spectrum. The green curve represents the variation of the Planck Law maxima with effective temperature.

Chapter 2

Methodology

2.1 Calculating extinction ratio data

When observing stars through a photometric filter, only a small fraction of the bolometric stellar flux that reaches the telescope is detected. This is due to the design of the filter in question, which determines the fraction of photons detected at a given wavelength, known as the transmittance. The variation in transmittance as a function of photon wavelength is known as a transmission curve, bandpass or filter response function. Examples of filter response functions for the photometric systems are given in Figures 2.2-2.5. It is clear that range of wavelengths for which the transmittance is non-zero is very narrow when compared to the full EM spectral range.

Stars, as mentioned earlier, emit photons with wavelengths across the full EM spectrum. Figure 1.2 shows that the difference between absolute monochromatic stellar flux for different effective temperatures itself varies significantly as a function of wavelength. Therefore, when the distance to a star is unknown, a simple photometric flux measurement alone cannot easily distinguish the effect on the flux due to the intrinsic nature of the star from effects due to distance or extinction. This observational problem must therefore be mitigated before an accurate value of the extinction can be determined. The mitigation is carried out by calculating bolometric corrections.

The use of bolometric corrections requires the detailed knowledge of stellar spectra least susceptible to significant extinction, meaning, in effect, nearby stars. Knowledge of the spectrum from a reference star can allow the true spectrum of distant stars, with unknown extinction, to be calculated. The spectra of these stars can be computed by using a grid of predicted fluxes from a stellar atmosphere model, the grid being composed of the stellar parameters known to change emission in stellar atmospheres. These are effective temperature, surface gravity and metallicity. For all filter systems studied in this project, the nearby bright star Vega (α Lyr) was used as the reference object. Using Vega as the reference star is the most well-known approach to photometric calibration (Casagrande & Vandenberg, 2014).

After accounting for the effect of interstellar extinction on an object's emission, its apparent magnitude in the wavelength range of a given filter X , defined as increasing from the shortest (λ_1) to the longest (λ_2) wavelength for which its response function is non-zero, can be calculated as:

$$m_X = -2.5 \log_{10} \left(\frac{\int_{\lambda_1}^{\lambda_2} f_\lambda (10^{-0.4A_\lambda}) S_\lambda d\lambda}{\int_{\lambda_1}^{\lambda_2} f_\lambda^0 S_\lambda d\lambda} \right) + m_X^0 \quad (2.1)$$

where f_λ represents the (theoretical) monochromatic flux at a given wavelength λ at the observer's distance from the source, A_λ is the extinction in X as a function of wavelength (see Equation 2.7 later for calculation of values from the Cardelli et al. (1989) law), S_λ represents the filter response function of X , example of which are given in Figures 2.2-2.5, and f_λ^0 and m_X^0 represent the monochromatic flux and apparent magnitude, respectively, in X of a known reference object, which is Vega in the case of the system used in this project. The use of these two well-determined observational parameters allows the remaining (uncertain) terms to be fixed to a known scale.

To derive the equation linking a bolometric correction with the extinction parameter, we start with the definition of a bolometric correction in a filter X , which is denoted by BC_X :

$$BC_X \equiv M_{\text{bol}} - M_X \quad (2.2)$$

where M_X is the absolute magnitude of the object in X and M_{bol} is its (predicted) absolute bolometric magnitude, defined relative to the Sun using:

$$M_{\text{bol}} = M_{\text{bol},\odot} - 2.5 \log_{10} \left(\frac{4\pi R^2 F_{\text{bol}}}{L_\odot} \right) \quad (2.3)$$

where F_{bol} is the bolometric stellar flux at its surface, R is the stellar radius, $M_{\text{bol},\odot}$ is the solar absolute bolometric magnitude, which is assumed in this work to have a value of 4.75 and L_\odot is the solar luminosity, for which a value of $3.844 \times 10^{33} \text{ erg s}^{-1}$ is used. Bolometric corrections can be expressed as a function of extinction using the definition of M_X in terms of m_X and the distance d to the source:

$$M_X = m_X - 2.5 \log_{10} \left(\left(\frac{d}{10\text{pc}} \right)^2 \right), \quad (2.4)$$

together with the equation linking flux definitions to distance:

$$f_\lambda d^2 = F_\lambda R^2 \quad (2.5)$$

where F_λ is the monochromatic flux at λ at the stellar surface. This gives the final function for a bolometric correction (BC) for filter X :

$$\begin{aligned}
BC_X = M_{\text{bol},\odot} - m_X^0 - 2.5 \log_{10} \left(\frac{4\pi R^2 F_{\text{bol}}}{L_{\odot}} \right) \\
+ 2.5 \log_{10} \left(\frac{\int_{\lambda_1}^{\lambda_2} F_{\lambda} (10^{-0.4A_{\lambda}}) S_{\lambda} d\lambda}{\int_{\lambda_1}^{\lambda_2} f_{\lambda}^0 S_{\lambda} d\lambda} \right)
\end{aligned} \tag{2.6}$$

It should be noted that F_{λ} is the monochromatic spectral flux produced by the theoretical stellar atmosphere model, and varies with changes in the effective temperature, surface gravity and metallicity of the model. For a filter X , the extinction parameter A_X , equal to A_{λ} for the response function of filter X , is usually parametrised relative to the extinction in the well-studied Johnson- V filter, A_V . To extract A_X , we use the simple relation

$$A_{\lambda} = \left(\frac{A_{\lambda}}{A_V} \right) A_V \tag{2.7}$$

together with the Cardelli et al. (1989) extinction law for A_{λ}/A_V , which is monochromatic and therefore must be placed within the integrand of Equation 2.6. Given that the Cardelli et al. (1989) extinction law is normalised to A_V , the value of A_V must be specified prior to the calculation of the bolometric correction. Equation 2.6 was implemented twice, once for each of two distinct A_V values (for this project these were $A_V = 0, 1$). It should be noted that $BC_X(A_V = 0)$ essentially assumes no extinction in any filter. Two output values were calculated for Equation 2.6, one for each A_V value. The difference between the two outputs was then taken to extract the extinction ratio A_X/A_V , via the following equation (Girardi et al., 2008):

$$BC_X(0) - BC_X(A_V) = (A_X/A_V) A_V \tag{2.8}$$

As demonstrated in Equation 2.8, any dependence of the A_X/A_V data on the Vega measurements or (as yet unknown or uncertain) bolometric quantities from Equation 2.6 is eliminated during the subtraction. However, effects due to the nature of the atmosphere of the stellar source on the extinction ratio will remain present, in the form of the integration of $F_{\lambda} (10^{-0.4A_{\lambda}})$ and F_{λ} in the respective bolometric correction terms.

The Forbes effect (see Section 1.2.2) has an impact on the non-zero A_V value chosen for Equation 2.8 because if R_V is held constant at the standard diffuse ISM value of 3.1 (Cardelli et al., 1989), a larger A_V value implies a longer path through the ISM, and thus a stronger Forbes effect. According to Girardi et al. (2008), any significant impact from the Forbes effect on the values of A_X/A_V occurs for a chosen $A_V \gtrsim 4$. They found that the effect was particularly strong for stars with $T_{\text{eff}} \lesssim 3000\text{K}$ and that, unsurprisingly, it became greater as the wavelength range covered by the filter response function increased.

Once the A_X/A_V data was calculated, functions of the three stellar parameters described in Section 1.2.1 were created and fitted to the data, with the function coefficients acting as the free parameters to be fitted. The best-fit values of these coefficients were calculated using a least-squares fit algorithm.

2.2 Software used

2.2.1 Isochrones

The isochrones used in this project were generated using the latest Bag of Stellar Tracks and Isochrones (BaSTI) web interface (Pietrinferni et al. (2004), Hidalgo et al. (2018)). The filter systems whose throughput data were employed by BaSTI to generate the fluxes for the isochrones were ACS, WFC3 and Gaia-DR2. It should be noted that the WFC3 isochrone output for BaSTI does not include flux magnitudes for the F300X filter.

To obtain isochrones from the online database, the desired range of isochrone ages, initial metallicity and photometric filter system must be specified. Therefore, the values of these quantities are shared by all stellar objects in any given isochrone. The output from the BaSTI database for each model stellar object gives the model's initial mass and current mass (i.e. after a time equal to the isochrone age), together with the logarithms of the stellar luminosity in solar units ($\log(L/L_\odot)$) and of the effective temperature in K ($\log(T_{\text{eff}})$), followed by the absolute magnitudes (with zero extinction) of the object in each filter of the system.

2.2.2 Stellar atmosphere models

To generate the predicted stellar flux, pre-calculated ATLAS9 model stellar atmosphere spectra (Kurucz, 1993). The spectra came in the form of tables incorporated wavelengths, ranging from 9 nm to 160,000 nm, with a resolution of 2 nm or less in the UV, and the predicted monochromatic flux at those wavelengths. Each table, representing one stellar spectrum, is identified by the surface gravity, effective temperature and metallicity of the stellar atmosphere producing that spectrum. Table 1 of Castelli & Kurucz (2004) contains precise details of the coverage of the model atmospheres in $(T_{\text{eff}}, \log(g))$ parameter space, while a brief summary of the limits of the space is listed in Table 2.1. Four input metallicities were used for ATLAS9, at values of $[\text{Fe}/\text{H}] = -2, -1, 0$ and 0.5 , covering the metallicities of most observed globular and open clusters. The data for each metallicity values was subject to the same T_{eff} and $\log(g)$ coverage in ATLAS9.

Parameter / unit	Minimum	Maximum	Number of values
$T_{\text{eff}} / \text{K}$	3500	50000	76
$\log(g / \text{cm s}^{-2})$	0.0	5.0	11
[Fe/H]	-2.0	0.5	4

Table 2.1: Ranges for the input parameters for ATLAS9 atmospheric models

To make the results of this project apply to the greatest possible range of stellar types, the model atmospheres being employed must ideally be able to reproduce all observed stellar types. Since ATLAS9 atmospheres are constructed from a grid of T_{eff} and $\log(g)$ values (Castelli & Kurucz, 2004), the simplest method of ascertaining their applicability is to obtain the T_{eff} and $\log(g)$ values of the stellar objects which make up the isochrone.

However, the BaSTI data format for a given isochrone does not include explicit values of the surface gravities or radii of the constituent stars. Therefore, to derive the surface gravity g of a given star, we must combine Equation 1.11, to derive the stellar radius, and Equation 1.13, resulting in the following definition of g :

$$g = \frac{4\pi G M_* \sigma_{\text{SB}} T_{\text{eff}}^4}{L_*} \quad (2.9)$$

After this had been completed for all stars in an isochrone, each star had a co-ordinate in $(T_{\text{eff}}, \log(g))$ parameter space, plus the metallicity of the overall isochrone model. These co-ordinates were then plotted over the grid of co-ordinates for which ATLAS9 spectra were available, as listed in Table 1 of Castelli & Kurucz (2004). The results are shown in Figure 2.1, using stars in isochrones with ages of 50 Myr (red points) and 12 Gyr (black points). The blue points represent the ATLAS9 model grid, which, in fact, extends to the left beyond the T_{eff} -scale presented in the figure, up to a T_{eff} value of 50,000 K.

With the exception of the very coolest, and therefore faintest, main sequence stars in the bottom right of the figure, it is clear from Figure 2.1 that the ATLAS9 T_{eff} - $\log(g)$ grid covers the required parameter space for isochrones of all ages including extremely young and extremely old clusters. Any changes in the position of the isochrones in the $(T_{\text{eff}}, \log(g))$ plane at the plotted ages due to a change in metallicity were found to have an insignificant impact on the overlap between the ATLAS9 grid and both isochrones in the $(T_{\text{eff}}, \log(g))$ plane.

This near-complete coverage of stellar objects in isochrones at all ages allows the ATLAS9 data to be applied to the MSTO locations at all isochrone ages, which ensures the applicability of the best-fit isochrone parameter comparisons (see Section 2.4 later) to populations of all ages. Therefore, ATLAS9 is a suitable basis from which start

calculating bolometric corrections and therefore, via Equation 2.8, extinction.

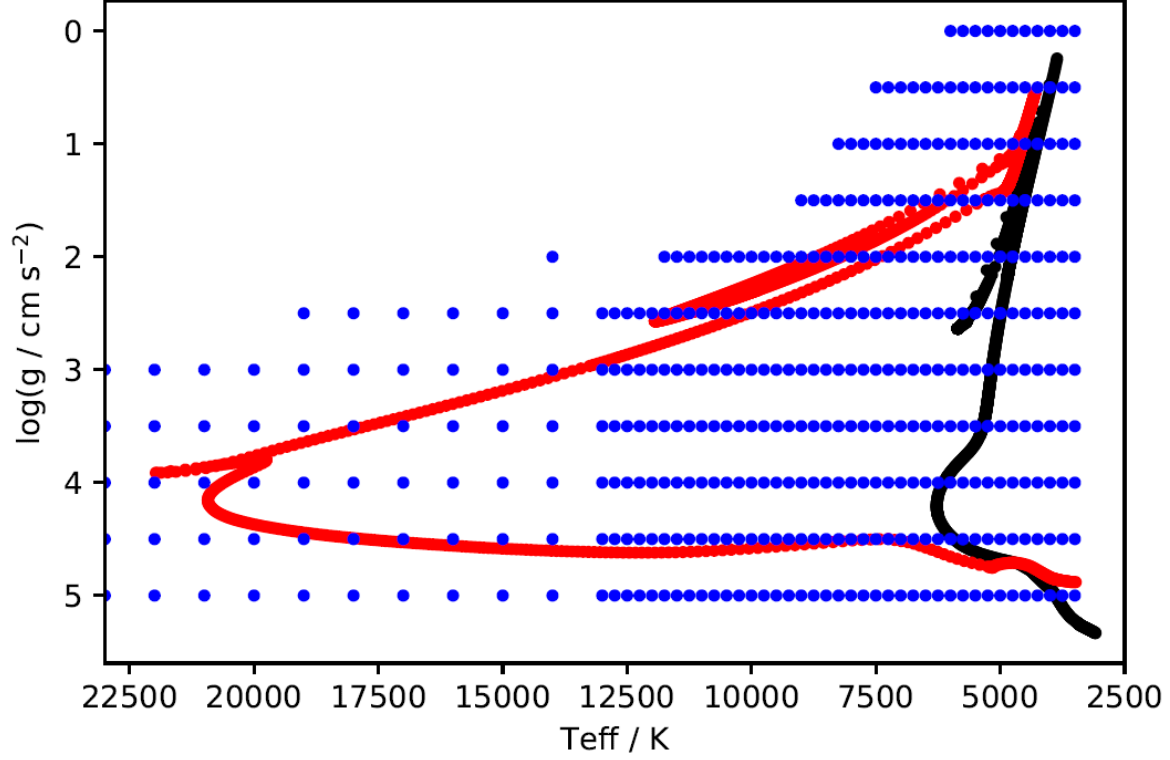


Figure 2.1: $T_{\text{eff}}\text{-}\log(g)$ scatter plot for a BaSTI 50 Myr, $[\text{Fe}/\text{H}] = -1$ isochrone (red), a BaSTI 12 Gyr, $[\text{Fe}/\text{H}] = -1$ isochrone (black) and ATLAS9 model grid (blue) for $T_{\text{eff}} \leq 23000$ K.

2.2.3 Programming languages

The tables of bolometric corrections were generated using a FORTRAN 77 code which incorporated Equations 2.2-2.8 and input data files with tables describing the response functions of all relevant filter systems (described in detail in Section 2.3) at the same wavelengths as those listed in the ATLAS9 model atmosphere tables, with the number of tables for each stellar metallicity value equal to the total number of $(T_{\text{eff}}, \log(g))$ combinations available.

Once the bolometric correction tables were produced, all subsequent processes, including the subtraction required to obtain A_X/A_V shown in Equation 2.8, were written in Python 2.7 in the form of an IPython notebook. The repository containing all data, plots and programme codes for this project can be found at https://github.com/AlexlwAstro/phd_work.

2.3 Filters studied

In this project, three broad-band filter systems were employed. Two are systems on board the Hubble Space Telescope (HST). These are the Advanced Camera for Surveys (ACS), installed in 2002 on the HST (Sarajedini et al., 2007), and the Ultraviolet Imaging Spectrograph channel of the Wide-Field Camera 3 (WFC3/UVIS), installed on the HST in 2009 (Kalirai et al., 2010; MacKenty et al., 2010). The third is the single set of three broadband filters mounted on the Gaia space observatory (Jordi et al., 2010), launched in 2013.

Examples of response functions for the three filter systems employed in this project are shown in Figures 2.2-2.5. By comparing these with the filters' information in Table 2.2, it can be seen that the exact shape of the response function has a significant impact on the observed flux, as shown in its contribution to the value of the apparent magnitude in Equation 2.1.

Reference will also be made to the Johnson-Morgan filter system (often simply known as the Johnson system) UBV Johnson & Morgan (1953), later extended as the Johnson-Cousins UBVRI Bessell (1990) system, which has been in use for decades and continues to be the standard reference for more modern filter systems. Of particular importance are the Johnson blue (B) and yellow (V) filters, as these formed the original benchmark for observing stellar populations and evolutionary stages.

The standard treatment of extinction is to apply a single constant value of the extinction ratio for a given filter X . This quantity is usually expressed as a fixed extinction ratio A_X/A_V of the (constant) coefficient value in the Johnson- V filter, the standard visual comparison filter. This value is maintained for all stars, regardless of the different effective temperatures, metallicities or surface gravities of the different types of stars present in any given population. The wavelengths of optical light lie between 3800 Å and 7400 Å, with the V filter having a central wavelength of 5500 Å.

In Table 2.2, all the filters used for this project are listed. The name of each filter is displayed alongside its central wavelength (λ_{cen}), full-width at half-maximum (FWHM) and the minimum (λ_{min}) and maximum (λ_{max}) detection wavelengths. Hence, when combined, these filters cover wavelengths from the soft-ultraviolet (soft-UV) to the near-infrared (NIR), including all visible wavelengths. The FWHM is defined as the difference between the lowest and highest wavelength values at which the transmittance value is half of its maximum value for the filter, typically assuming the response function can be approximated as a Gaussian distribution centred on the central wavelength. The FWHM acts as an approximate measure of the wavelength range within which the filter can be used for observations.

System	Filter	$\lambda_{\text{cen}} / \text{\AA}$	FWHM / \AA	$\lambda_{\text{min}} / \text{\AA}$	$\lambda_{\text{max}} / \text{\AA}$
ACS	F435W	4359	881	3610	4860
	F475W	4781	1403	3863	5563
	F555W	5413	1236	4584	6209
	F606W	5961	2255	4634	7180
	F625W	6323	1390	5446	7100
	F775W	7763	1517	6804	8632
	F814W	8117	2096	6885	9648
WFC3	F218W	2216	329	1990	2603
	F225W	2341	464	1990	2968
	F275W	2696	417	2282	3119
	F300X	2722	660	2137	4098
	F336W	3368	550	3014	3707
	F390W	3929	951	3255	4470
	F438W	4322	674	3895	4710
	F475W	4768	1482	3942	5582
	F555W	5262	1578	4381	7045
	F606W	5941	2298	4700	7204
	F625W	6274	1573	5414	7138
	F775W	7725	1454	6869	8571
	F814W	7814	1505	6978	9684
Gaia	G	6631	4397	3321	10515
	G_{bp}	5330	2530	3283	6714
	G_{rp}	7896	2956	6296	10637

Table 2.2: Basic properties of the filters employed in this project. See text for details. Source: <http://svo2.cab.inta-csic.es/svo/theory/fps3/index.php>

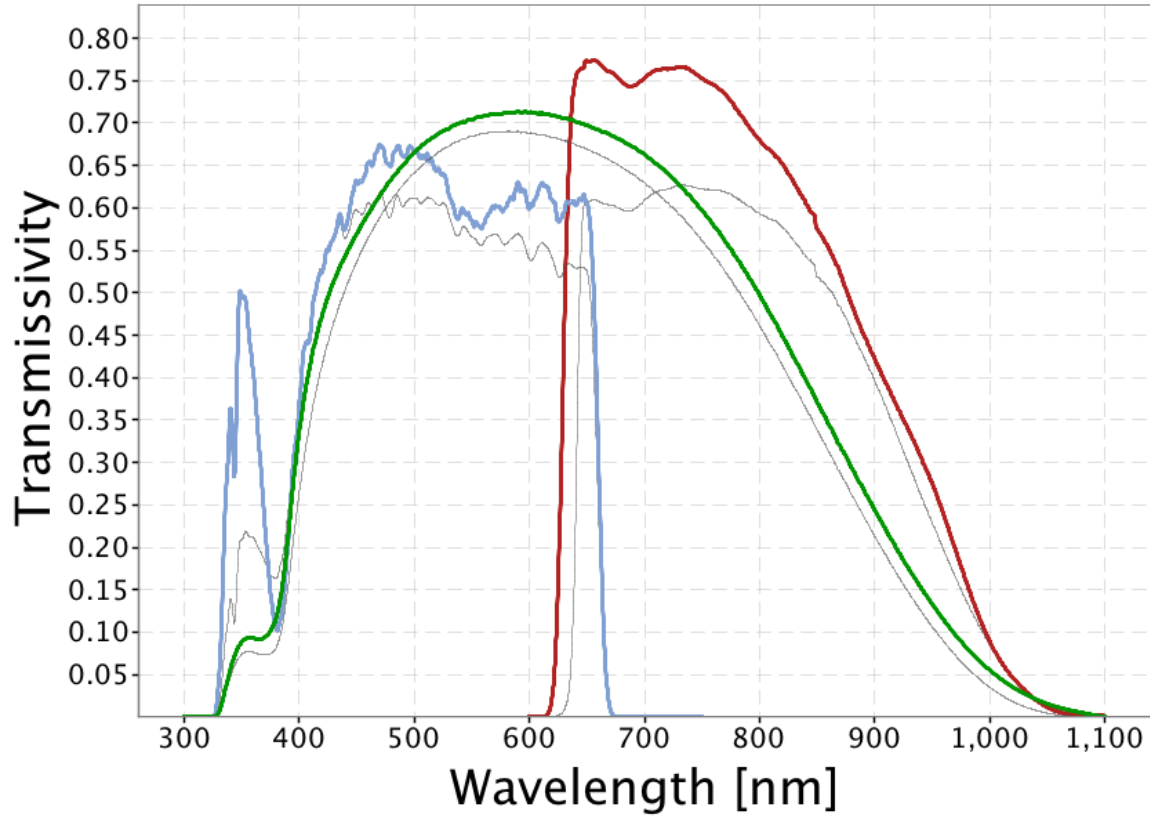


Figure 2.2: Filter response functions for Gaia photometric filters. Source: https://www.cosmos.esa.int/web/gaia/iow_20180316

2.4 Isochrone data fitting

To match the quantities of observational datasets (with unknown extinction) and isochrones, it is necessary to correct the observational data for distance and add extinction to the isochrones. This is that standard procedure used when analysing observational data. Thus, the $M_{\text{ext},X}$ values for the isochrones and the observational data are being compared. The functions described in Section 3.3 were then applied to the dataset of stellar objects, producing values of $M_{\text{ext},X}$ for each filter for all objects, as is the standard for analysing observational data with unknown extinction values.

When comparing the two approaches to extinction, in order to test for any differences in projected isochrone age via the MSTO, a range of ages must be considered. A “primary” age was utilised as the true cluster isochrone age. This primary isochrone was subjected to both the function-based (FBER) and fixed extinction-ratio approaches. Two isochrones with ages equidistant from the primary were subjected to the standard fixed-extinction approach only. All four of the resulting $M_{\text{ext},X}$ isochrones were plotted together in the four chosen CMD axes, together with the original (zero-extinction) isochrone for visual reference.

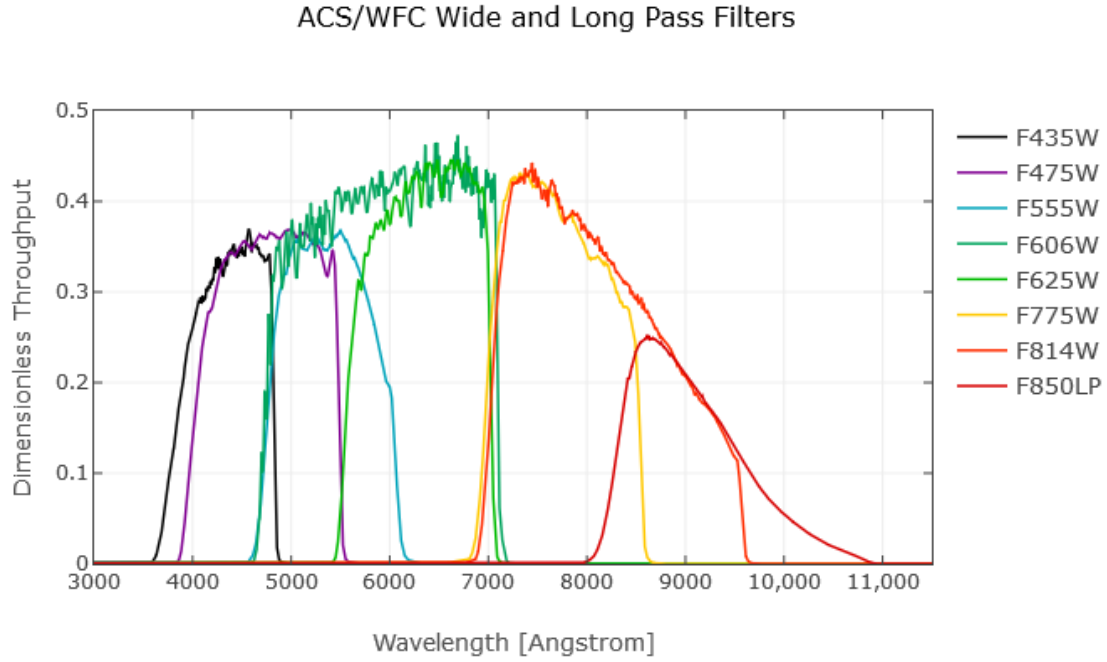


Figure 2.3: Filter response functions for wide-field ACS filters. Source: <http://www.stsci.edu/hst/acs/analysis/throughputs>

This procedure was employed for two values of A_X/A_V for the fixed-extinction treatment. Both were extracted from the ATLAS9 data tables for a $\log(g)$ value of 5.0 to represent a main-sequence star, which is suitable when MSTO positions are being compared. Given the large number of filters studied in this project, four commonly-used CMD axes were selected to test for any effects of a A_X/A_V function. Two of these are specific to the WFC3 system, with one CMD each for ACS and Gaia.

2.5 Observational test case: NGC 6793

To test the effects of the two different treatments of A_X/A_V on observational data, both were employed to predict the isochrone parameters (age, [Fe/H] and A_V) for the open cluster NGC 6793.

NGC 6793 has little information available in the literature when compared to open clusters. Three observational studies have been published which give estimates for the properties of the cluster. The basic properties for all three studies are listed in Table ???. However, it has the significant advantage of having both a very high A_V extinc-

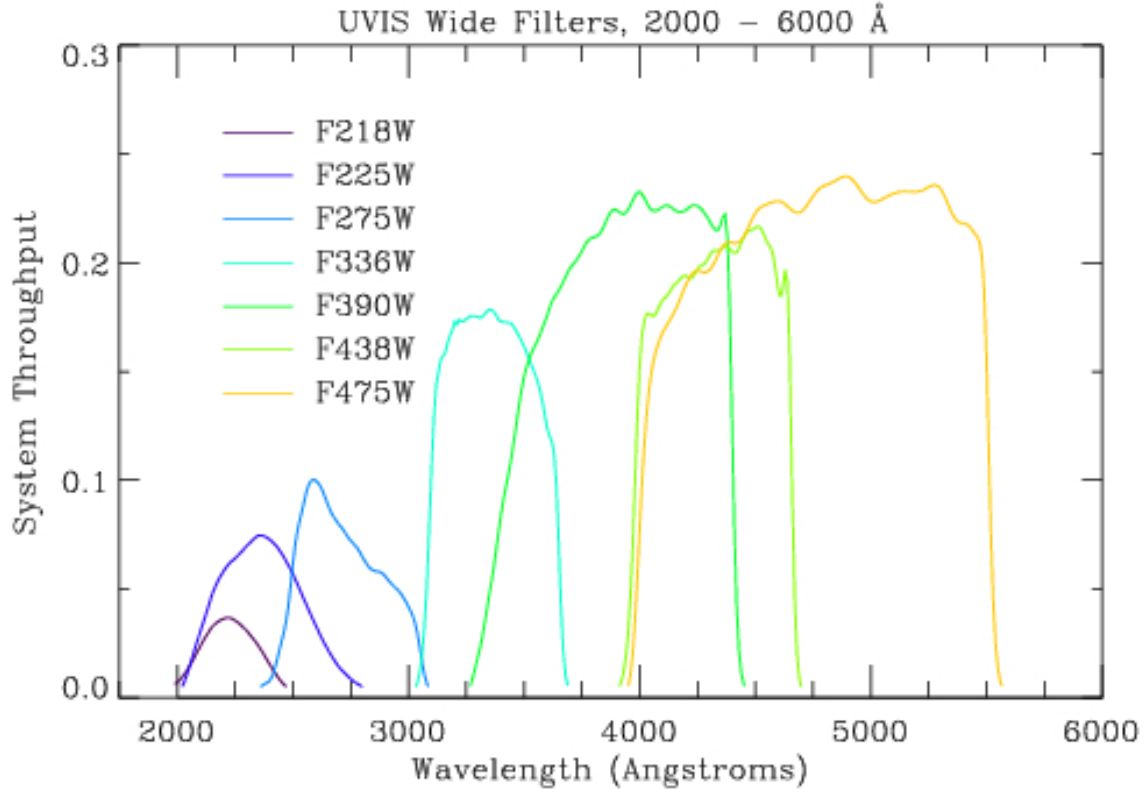


Figure 2.4: Filter response functions for wide-field WFC3 filters. Source: http://www.stsci.edu/hst/wfc3/ins_performance/throughputs/UVIS_filterthru.html

tion value among star clusters and a full set of Gaia parallax measurements for its member stars. The accurate distances to all its members allows for a higher degree of confidence in the position of the observed cluster CMD. Meanwhile, a high A_V value increases any disagreement between the extinction treatments being compared for the cluster. Consequently, any resulting disagreement in estimates of the best-fit isochrone parameters for the cluster become greater and more significant.

The Gaia DR2 dataset for NGC 6793, containing the parallaxes and apparent magnitudes (in all three Gaia filters) for 338 objects identified as belonging to the cluster, was obtained. The number of objects is greater than the 271 photometric Gaia objects found by Gaia Collaboration et al. (2018), hereafter referred to as GC18. Restrictions on the parallax measurements were implemented, by imposing a distance-based selection range centred at 600 pc, which was treated as the centre of the cluster, in line with the GC18 estimate in Table ?? . The range was decreased until the remaining sample size was approximately equal to 271. When this was implemented, the final sample of observational data for NGC 6793 contained 274 objects. Some of these objects still

Isochrone (Age/Myr , [Fe/H])	T_{eff} minimum	T_{eff} maximum	$\log(g)$ minimum	$\log(g)$ maximum
500,0.002	2870	9640	0.886	5.137
1000,0.002	2824	8035	1.608	5.184
5000,-1.049	3118	7112	0.456	5.318
10000,-1.049	3086	6412	0.286	5.332

Table 2.3: Ranges of effective temperature and surface gravities in selected BaSTI isochrones

Cluster property	K05	K13	GC18
Distance modulus / mag	10.73	9.399	8.894
-> distance / pc	1400	724	601
log(age / yr)	8.64	8.695	8.78
-> Age / Myr	437	495	603
$E(B - V)$ / mag	0.17	0.312	0.272
-> A_V / mag (if $R_V = 3.1$)	0.53	0.967	0.843
[Fe/H]	?	?	?
Members	? (> 3 ACSS-2.5)	133*	465 (271 with Gaia photometry)

*number of 1σ objects inside MWSC "cluster corona border"

Table 2.4: Observational parameters for NGC 6793, according to Kharchenko et al. (2005) (K05, WEBDA archive page), Kharchenko et al. (2013) (K13, VizieR archive page) and Gaia Collaboration et al. (2018) (GC18), respectively.

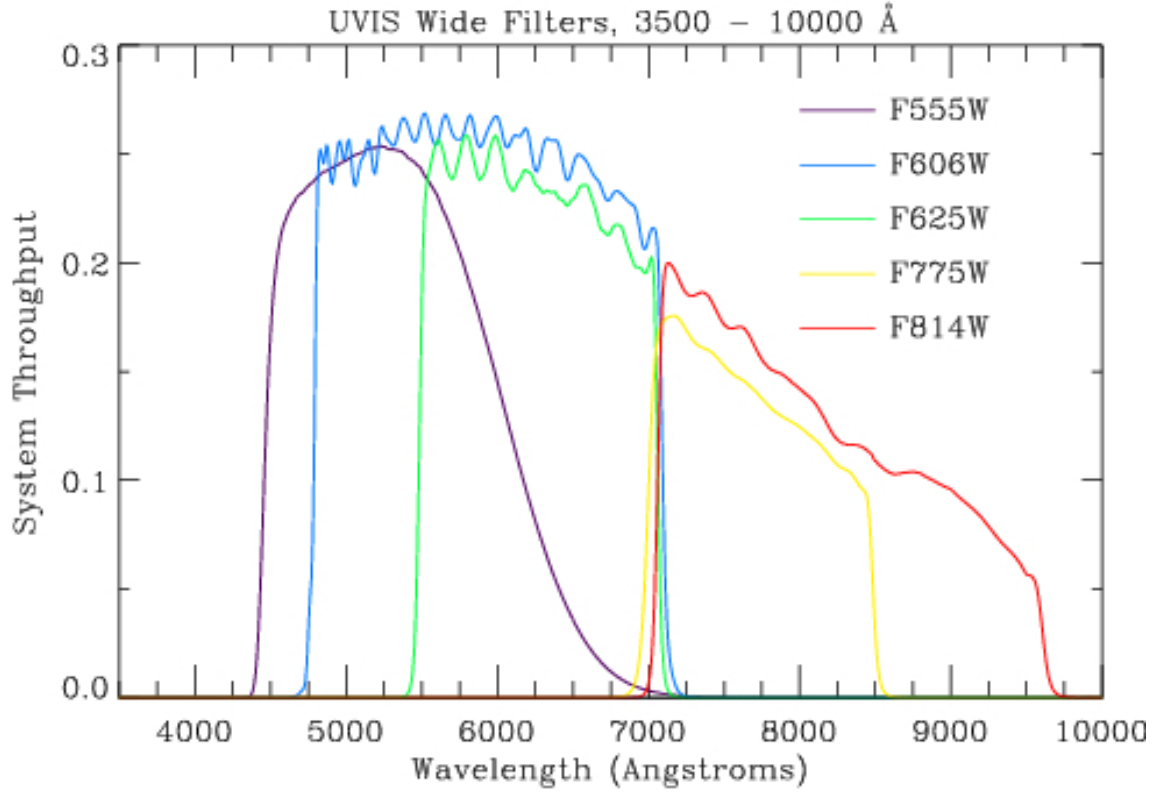


Figure 2.5: Filter response functions for wide-field WFC3 filters. Source: http://www.stsci.edu/hst/wfc3/ins_performance/throughputs/UVIS_filterthru.html

had parallax distances further from the cluster centre than would be expected for any star cluster. The size of the final dataset balanced the need for maintaining sufficient data points, to achieve a valid comparison to the previous studies of NGC 6793, particularly GC18, and eliminating the most anomalous data, such as stars with parallaxes calculated as being negative (and therefore not physically feasible).

The isochrone fitting to the NGC 6793 was done by eye using a plot of the cluster’s observed Gaia CMD, the position of each star corrected for its parallax distance. Using the values of $E(B-V)$ and age from GC18, a standard-case isochrone was derived, again assuming a diffuse ISM (i.e., $R_V = 3.1$). The standard treatment was employed twice, creating a different isochrone each time. A coefficient calculated from $(A_X/A_V)_{MS}$ was applied in one case and one calculated using $(A_X/A_V)_{plat}$ in the other. The fitting process was carried out in sequential stages:

1. First, the upper main sequence of the FBER isochrone was fitted to that of the standard-case isochrone by varying the value of A_V used to calculate the final FBER value for each stellar object.

2. Next, the age of the FBER isochrone was varied to match the observed turn-off location in the NGC 6793 data as far as possible.
3. Finally, the FBER isochrone metallicity was varied in an attempt match the observed lower main-sequence.

The isochrone with the resulting parameters were then plotted alongside two standard-case isochrones, The resulting curves were compared to each other for accuracy with respect to the observational data.

Chapter 3

Results and discussion

3.1 Choice of R_V and A_V values

In order to generate the bolometric correction data, the Fortran software required the user to input a single, global value for the parameters R_V and A_V . The global R_V value, which is applied to the Cardelli et al. (1989) monochromatic extinction law, was chosen as $R_V = 3.1$. This is equal to the mean diffuse ISM value calculated by Rieke & Lebofsky (1985) and widely used in analysis of stellar observations. The choice for the non-zero value of A_V was required in order to generate the A_X/A_V data via Equation 2.8. The choice for this global value was made as $A_V = 1.0$. This was chosen for multiple reasons:

- The value is sufficiently large for differences between both BC datasets to become apparent in the A_X/A_V data.
- The A_V values of observed stellar populations are often around or less than 1.0, which precludes using a higher value for the BC data.
- A value of $A_V = 1.0$ is also sufficiently small for the Forbes effect (see Section 1.2.2 to have a negligible impact, even for filters with the widest bandwidths.

3.2 Trends in A_X/A_V data

For all filters, the greatest variations in A_X/A_V data occur with changes in T_{eff} , with changes due to $\log(g)$ and $[\text{Fe}/\text{H}]$ being much less significant. This is to be expected, given that the value of T_{eff} has a significant effect on the magnitude and shape stellar spectral energy distribution (see Figure 1.2), while the effects of the surface gravity and metallicity are restricted to the absorption lines in the SED.

Another general feature is the convergence of A_X/A_V to a single maximum value in each filter, at $T_{\text{eff}} = 50,000$ K, for higher effective temperatures, independent of

metallicity and surface gravities. In most filters, this convergence is achieved to within a margin of 0.01 from the value at $T_{\text{eff}} = 50,000$ K by temperatures of 20,000 K. The region of parameter space in T_{eff} , $\log(g)$ and $[\text{Fe}/\text{H}]$ characterised as having achieved this convergence is referred to henceforth as the “high- T_{eff} plateau region” or simply “plateau”.

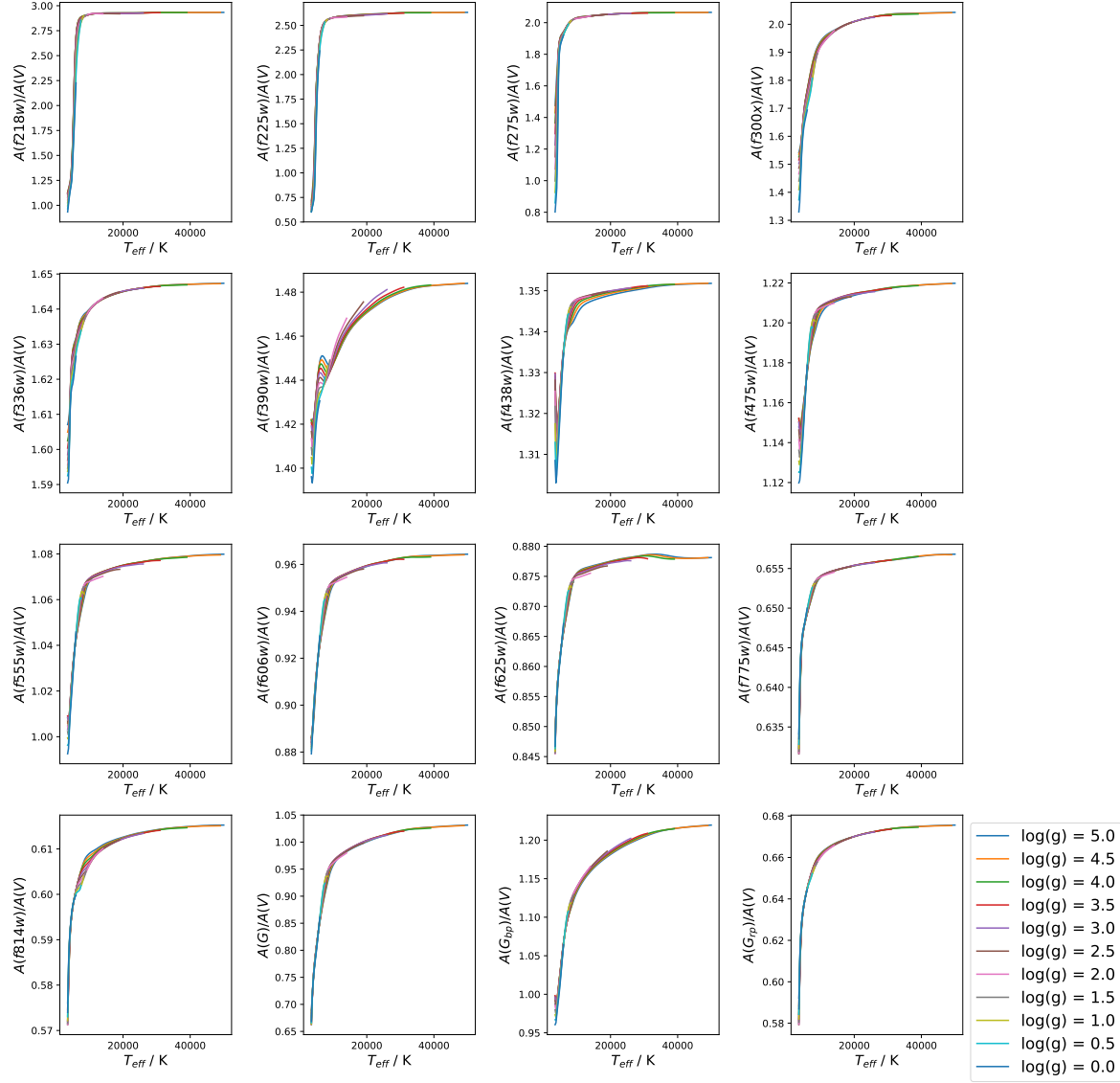


Figure 3.1: Solar-metallicity extinction ratio data for the WFC3 (first 13 panels) and Gaia (last 3) systems, with point-to-point lines connecting datapoints for a fixed $\log(g)$ value.

A property found in the data for some filters, more pronounced at higher metallicity but with a possible slight dependence on surface gravity, is the tendency of the

gradient of A_X/A_V with increasing T_{eff} to become significantly less positive at the lowest temperatures in the data, typically around 4000K and below. The spread in A_X/A_V values for different $\log(g)$ is typically about 0.2-0.4, with a linear progression from $\log(g) = 5.0$ at the lowest end to $\log(g) = 0.0$ at the highest. In some filters, at the highest metallicity employed ($[\text{Fe}/\text{H}] = 0.5$), this phenomenon causes the gradient to invert and become significantly negative, reversing the trend everywhere else in the data, including for the same filters at lower metallicity. Due to the shape of the resulting point-to-point line in these axes, it has been dubbed the “tail-flick” phenomenon.

This gradient inversion was ignored as an artefact from the numerical integration required for Equation 2.6. This was justified on the basis that it is physical infeasible for a cooler star to experience a higher extinction A_X than a hotter star for a globally-constant A_V value and metallicity, as was assumed for data in each BC table. In the relevant filters, only effective temperatures above those affected by the gradient inversion was used for fitting.

3.3 Extinction ratio models

In order to find usable model functions without running into issues with degeneracy between coefficients in the same function, prioritising the order in which the three stellar parameters were model was paramount. Too many coefficients created errors that were significantly greater in degenerate coefficients than in non-degenerate ones. This would obscure any useful information about the validity of the function form.

The bolometric flux of a black body can be calculated as the total area under the curve described by the Planck function per unit wavelength/frequency as a function of wavelength/frequency (see Equations 1.9 and 1.10). Since stellar emission spectra can be reasonably approximated by a black body emission with absorption lines, it can be seen from Equation 1.11 that the greatest effect on stellar spectra, and therefore on the extinction, will come from changes in effective temperature. Therefore, the initial functions to be fitted were simple functions of T_{eff} only:

$$A_{\text{pow}}(T_{\text{eff}}) = a(T_4)^b + c \quad (3.1)$$

$$A_{\text{exp}}(T_{\text{eff}}) = a \exp(bT_4) + c \quad (3.2)$$

where $T_4 = 10^{-4} \times T_{\text{eff}}$. The fitting operation was carried out on the data for solar metallicity ($[\text{Fe}/\text{H}] = 0.0$) and, because it gave the greatest number of T_{eff} data points, $\log(g) = 5.0$. This dataset will be referred to as the basic fitting data (BFD).

****The results of this fitting process are detailed, for the cases where the fit was sufficiently accurate, in Table 3.1. The table shows the filters and lists which of the two

function forms provided the best fit for the relevant data, followed by the respective coefficient values and uncertainties. The final column lists the lowest T_{eff} value for which the given coefficient values is valid at all combinations of surface gravity and metallicity.

For the data in the Gaia filters, the opportunity was taken to compare the models produced in this project with the models for R_X for these same filters detailed by Casagrande & Vandenberg (2018). To apply the Casagrande & Vandenberg (2018) model to the extinction ratios used for this project, the definition of R_X was used to construct the following equation:

$$\frac{A_X}{A_V} = \frac{R_X}{R_V} = \frac{R_X}{3.1} \quad (3.3)$$

****Within the metallicity and temperature ranges for which the Casagrande & Vandenberg (2018) model is applicable, these models are in agreement with the ATLAS9 A_X/A_V and with the models created for this project.

There were filters whose BFD could not support an accurate fit or maintain the desired accuracy across all combinations of $\log(g)$ and $[\text{Fe}/\text{H}]$ using A_{pow} or A_{exp} . For these filters, more intricate functions were sought, including functions with explicit dependences on g and $[\text{Fe}/\text{H}]$. Several unsuccessful approaches were made before an acceptable function was found for each filter.

The most successful approach was plotting all the available data for each filter, in multiple 2D and 3D axes, and analysing it visually. The trends seen in the data were transcribed to find not only an overarching function template, akin to the status of A_{pow} and A_{exp} , but also smaller mathematical constructs within the template, such as describing a decay coefficient in terms of $\log(g)$ and $[\text{Fe}/\text{H}]$.

The details of the final form of the template as a function of each stellar parameter were deduced by fitting a logistic function of T_{eff} to the A_X/A_V data for each ($[\text{Fe}/\text{H}], \log(g)$) combination. This was decided on the basis that A_{exp} had been superior to A_{pow} in describing the data for these filters and because the low- T_{eff} change in gradient appeared to be more significant than for other filters. Furthermore, the gradient was not inverted, as can be seen in Figure 3.1. Of particular importance was the fact that the T_{eff} gradient prior to the plateau appears to lead to an asymptote at lower, but still physically-viable, stellar effective temperatures. This issue is resolved by the logistic function's property of converging to a constant value for both very high and low values of the input variable.

For a general logistic function in T_{eff} , there are four key parameters:

- The global maximum value, denoted in this case by A_{max} ;
- The global minimum value, A_{min} ;

- The exponential decay coefficient, k ;
- The T_{eff} -coordinate of the sigmoid midpoint, in this case T_0 .

It was confirmed that this new function could describe each scenario accurately enough for further analysis, ****as shown in Table 3.2. The resulting coefficients were tabulated and analysed for trends and, if found, the nature of those trends. This allowed for the incremental construction of sub-functions of $\log(g)$ and $[\text{Fe}/\text{H}]$, making the overall function, A_{logis} , sensitive to all three input stellar atmosphere parameters, with effective temperature having the greatest effect and the relative effects of the other parameters dependent on the best-fit values of the relevant coefficients.

The sub-functions of $\log(g)$ and $[\text{Fe}/\text{H}]$, upon inspection of the coefficients for the T_{eff} -only logistic function, were found to be simple functions of $\log(g)$ and $[\text{Fe}/\text{H}]$, independent of T_{eff} variations. This allowed for them to be used as the definitions of T_0 and k , as shown in Equations 3.4 and 3.5, respectively.

$$T_0 = a \log(g) + b \left(\frac{[\text{Fe}/\text{H}]}{|[\text{Fe}/\text{H}]|^{1/2}} \right) + c \quad (3.4)$$

$$k = d \log(g) + e [\text{Fe}/\text{H}] + f \quad (3.5)$$

$$A_{\text{logis}}(T_{\text{eff}}, g, [\text{Fe}/\text{H}]) = \frac{(A_{\text{max}} - A_{\text{min}})}{(1 + \exp(-10^{-4}k(T_{\text{eff}} - T_0)))} + A_{\text{min}} \quad (3.6)$$

The final form was then subjected to a final fit on the entire A_X/A_V dataset, covering the entire $(T_{\text{eff}}, \log(g), [\text{Fe}/\text{H}])$ parameter space available. A_{logis} was able to accurately reproduce the behaviour of almost the entire dataset. The coefficients for Equations 3.4-3.6 are given in Table 3.2.

The extinction-ratio data for all filters, with the exception of the four fully-UV filters in the WFC3 system, could be accurately modelled by the simplest functions trialled for fitting, $A_{\text{exp}}(T_{\text{eff}})$ or $A_{\text{pow}}(T_{\text{eff}})$.

All the functions are consistent with the general trends predicted by the physics in stellar atmospheres, since the effective temperature has the greatest effect upon the value of A_X/A_V , with relatively minor effects due to spectral absorption lines, via surface gravity and metallicity. In general stars with higher effective temperatures (and consequently stronger and bluer flux spectra) experience higher A_X/A_V values in all filters than stars with low effective temperatures. The maximum A_X/A_V value in a given filter decreases as the filter's central wavelength increases. This is expected for black-body analogues (see Equation 1.9 and Figure 1.2). Both trends are also consistent with the known short-wavelength preference of physical mechanisms causing interstellar extinction.

System	Filter	Function (A_{pow} or A_{exp})	Coefficients			T_{min} / K (global maximum error margin)
			a	b	c	
ACS	F435W	exp	-0.144 ± 0.031	-2.159 ± 0.360	1.352 ± 0.002	3500(0.03)
	F475W	exp	-0.214 ± 0.047	-2.660 ± 0.380	1.226 ± 0.002	4000(0.025)
	F555W	exp	-0.0914 ± 0.048	-2.677 ± 0.901	1.045 ± 0.002	3500(0.01)
	F606W	exp	-0.218 ± 0.055	-2.867 ± 0.445	0.959 ± 0.002	3500(0.01)
	F625W	exp	-0.072 ± 0.078	-3.332 ± 2.000	0.865 ± 0.002	3500(0.01)
	F775W	pow	-0.0035 ± 0.0042	-1.4878 ± 1.5414	0.6507 ± 0.0031	3500(0.01)
	F814W	pow	-0.007 ± 0.005	-1.374 ± 0.830	0.611 ± 0.003	3750(0.015)
WFC3	F336W	pow	-0.0074 ± 0.0041	-1.5251 ± 0.7272	1.6478 ± 0.003	3500(0.025)
	F390W	exp	-0.0695 ± 0.0057	-0.6438 ± 0.177	1.489 ± 0.005	4500(0.04)
	F438W	exp	-0.1132 ± 0.0658	-3.0839 ± 1.0322	1.3504 ± 0.0017	3750(0.015)
	F475W	pow	-0.0179 ± 0.0037	-1.718 ± 0.275	1.220 ± 0.003	4000(0.02)
	F555W	pow	-0.0138 ± 0.0033	-1.8873 ± 0.3326	1.0798 ± 0.0024	3750(0.02)
	F606W	exp	-0.2131 ± 0.0559	-2.8788 ± 0.4604	0.9623 ± 0.0017	3500(0.015)
	F625W	pow	-0.0042 ± 0.0031	-2.0634 ± 1.0248	0.8787 ± 0.0022	3500(0.01)
	F775W	pow	-0.0033 ± 0.0041	-1.529 ± 1.6335	0.6568 ± 0.003	3750(0.01)
Gaia	F814W	pow	-0.0071 ± 0.0046	-1.3905 ± 0.8027	0.6158 ± 0.0034	4000(0.01)
	G	pow	-0.0888 ± 0.0045	-1.402 ± 0.0642	1.0395 ± 0.0033	****0(0.0)
	G _{bp}	pow	-0.115 ± 0.0081	-0.8997 ± 0.0692	1.2468 ± 0.0068	****0(0.0)
	G _{rp}	pow	-0.0159 ± 0.0047	-1.3519 ± 0.3678	0.6772 ± 0.0035	****0(0.0)

Table 3.1: Coefficient values produced for each filter via A_{exp} or A_{exp} fitting, as appropriately labelled. Any filters missing from this table are those with data that could not be accurately fitted using either function. The errors are calculated using a simulated A_X/A_V uncertainty of 0.01. ****The final column displays the lowest effective temperature for which the given model and coefficients were able to describe the A_X/A_V data across all values of $\log(g)$ and $[\text{Fe}/\text{H}]$

Coefficient	Filter			
	F218W	F225W	F275W	F300X
a	-120.9 ± 4.1	-97.21 ± 3.85	-239.0 ± 12.0	-302.1 ± 45.0
b	467.6 ± 7.9	357.2 ± 7.9	236.0 ± 20.4	350 ± 125
c	5673 ± 16	4967 ± 22	4161 ± 79	4270 ± 913
d	1.435 ± 0.209	-0.174 ± 0.136	-2.117 ± 0.326	-0.176 ± 0.087
e	-3.211 ± 0.382	-2.691 ± 0.256	-2.140 ± 0.445	-0.352 ± 0.115
f	19.19 ± 0.62	18.62 ± 0.55	22.20 ± 1.48	4.315 ± 0.529
A_{min}	1.026 ± 0.012	0.337 ± 0.028	0.409 ± 0.113	1.000 ± 0.199
A_{max}	2.909 ± 0.003	2.581 ± 0.003	2.030 ± 0.003	2.015 ± 0.004
Max. deviation in A_X/A_V	0.25	0.3	0.2	0.15

Table 3.2: Coefficient values for non-trivial A_X/A_V functions, as described in Equations 3.4-3.6, produced for fitting to UV filter data. The bottom row represents the global maximum deviation from the data.

The accuracy of these relatively simple functions is important because the A_X/A_V dataset for each filter is now reduced to a much smaller number of degrees of freedom, equal to the number of coefficients in the relevant function. The input parameters (T_{eff} , $\log(g)$ and $[\text{Fe}/\text{H}]$) are required regardless of whether interpolation of the tables of A_X/A_V data or the functions are being employed, and so they make no difference in comparing the information complexity of the tables versus the functions.

3.4 Effect on isochrones

The equations detailed in Section 2.4 were used to convert the model parameters listed in the BaSTI data to the stellar parameters used by the A_X/A_V functions in this project.

The ATLAS9 metallicity chosen for calculating the fixed-extinction A_X/A_V values to be applied to the isochrone was the value which best matched the metallicity of the isochrone to which the coefficient was applied. The ATLAS9 value will be denoted $[\text{Fe}/\text{H}]_{CM}$. The first value was equal to $(A_X/A_V)_{\text{plat}} = (A_X/A_V)(T_{\text{eff}} = 50,000\text{K}, \log(g) = 5.0, [\text{Fe}/\text{H}]_{CM})$, and the second was equal to $(A_X/A_V)_{MS} = (A_X/A_V)(T_{\text{eff}} = 5,000\text{K}, \log(g) = 5.0, [\text{Fe}/\text{H}]_{CM})$. This was done to reflect the fact that, for the first case, the assumption of a constant extinction value is valid in the plateau region and, for the second, the fact that, given the position of the MSTO in terms of stellar T_{eff} values, it would be more prudent to ensure that the upper main sequences resulting from both approaches to extinction coincide in the CMD, making it easier to see any disagreements in the turn-off ages. For each of these plots, A_V was fixed at a value of 1.0.

In each of the CMDs, the extinction ratio functions have been applied to a solar-metallicity ($[\text{Fe}/\text{H}] = 0$), 500 Myr isochrone, which is shown as a solid orange line. A fixed extinction ratio has been applied to three solar-metallicity isochrones with ages of 400 (solid green), 500 (solid blue) and 600 (solid red) Myr, respectively. A solar-metallicity, 500 Myr isochrone with zero extinction is added for illustration purposes as a solid purple line.

3.4.1 ACS

The CMD chosen for the ACS was the F435W-(F435W-F814W) axis combination. This CMD is useful as it pairs the bluest and reddest wide-field filters for the ACS in its colour index, which is the index most likely to distinguish between objects with a large range of effective temperatures, making it useful for modelling the main sequence and MSTO, the two most important CMD components for calculating cluster isochrone

ages. This CMD corresponds, by design, to the pre-existing Johnson-Cousins $B-(B-I)$ CMD (Sirianni et al., 2005), which allows direct comparison of observed data with archive data obtained before the creation of the HST filters.

It can be seen in Figure 3.3 that the impact of changing the extinction approach used to change the isochrone position in this CMD is insignificant. Although there are some larger differences in the position of the isochrone in the post-sub-giant branch (SGB) evolutionary stages, this is irrelevant when determining the isochrone age of an observed stellar population.

The result of using $(A_X/A_V)_{plat}$ is not significantly different from that of using $(A_X/A_V)_{MS}$ for this CMD. It can be seen that any changes in A_X/A_V values in the F435W and F814W ACS filters at different temperatures (see Figure 3.2) are insignificant compared to the range of magnitudes covered by the isochrones in Figures 3.3 and 3.4.

3.4.2 WFC3

Two different CMDs were chosen whose filters are part of the WFC3. The first CMD is the F555W-(F555W-F814W) axis combination. This CMD pairs a wide yellow filter (F555W) with the WFC3’s reddest IR wide-field filter. This CMD mimics the pre-existing and widely-used Johnson-Cousins $V-(V-I)$ CMD (Sahu et al., 2014), which allows direct comparison of observed data with archive data obtained before the creation of the HST filters.

As with the previous ACS CMD, this CMD shows no significant changes in isochrone position resulting from either employing a FBER model or changing the extinction ratio value used for the fixed-value extinction model from $(A_X/A_V)_{plat}$ to $(A_X/A_V)_{MS}$ or vice versa.

The second WFC3 CMD that was studied is the F814W-(F275W-F814W) axis combination. The filters that form this CMD cover the soft-UV and near-IR regions of the EM spectrum. The high baseline wavelength coverage of this combination of filters makes the colour index sensitive to differences in T_{eff} in the hot horizontal branch (HB) stars. These objects are important due to direct helium abundance measurements (from absorption lines) being available in globular clusters only for HB stars with $8000 \text{ K} \lesssim T_{\text{eff}} \lesssim 11500 \text{ K}$ (Lagioia et al., 2018).

In Figure 3.7, it can be seen that, when the models’ upper main sequences are aligned (i.e., the $(A_X/A_V)_{MS}$ fixed model is being used as a reference), the position of the MSTO of the FBER 500 Myr isochrone aligns with that of the 600 Myr fixed-ratio isochrone. By the point at which the SGB hook (Pols et al., 1998) appears, the FBER isochrone has almost realigned with the 500 Myr fixed-ratio isochrone. There are significant differences between the two 500 Myr isochrones after the lower portion of the

RGB. In the lower main sequence, all isochrones with fixed extinction ratios appear significantly redder, while more or less maintaining their F814W magnitudes. This can only be the result of significant differences in A_{F275W}/A_V values between models in the upper main sequence (higher T_{eff} values) and in the lower main sequence (lower T_{eff} values), as these differences are not reflected in the fixed-extinction models.

In Figure 3.8, the temperature of 50,000 K used for $(A_X/A_V)_{\text{plat}}$ increases the extinction ratio values in the fixed-extinction isochrones, shifting them down and to the right. Ironically, this higher T_{eff} value, which is far greater than any T_{eff} values present in the isochrone data, brings the MSTO positions of the two 500 Myr isochrones back into alignment. However, the use of $(A_X/A_V)_{\text{plat}}$ increases the lower main sequence gap between the fixed-extinction isochrones and the FBER example. The disagreement between the 500 Myr isochrones now begins earlier in the evolutionary cycle, at the base of the RGB.

Furthermore, there is a possibility of the lower main sequence disagreement between extinction treatment methods causing a disagreement in the estimated cluster metallicity, as the CMD position of this part of the isochrone is the most sensitive to changes in metallicity.

3.4.3 Gaia

The photometric filters in Gaia, as shown by their respective response functions in Figure 2.2, are designed such that the only useful colour index is the $(G_{\text{bp}} - G_{\text{rp}})$ index. The G filter, being the widest filter of the three available wide-field filters. This CMD is useful as it pairs the bluest and reddest wide-field filters for the ACS, which produces a larger range of spectral colours across all stellar masses, with the widest filter (G) being on the y-axis.

For the Gaia CMD, when $(A_X/A_V)_{\text{MS}}$ is used for the fixed-extinction isochrones, as shown in Figure 3.9, the turnoff position of the 500 Myr FBER isochrone appears to be lower on the main sequence than even the 600 Myr fixed-extinction case, suggesting that using the fixed-extinction treatment significantly and consistently over-estimates the isochrone age for an observed cluster. However, unlike the F814W-(F275W-F814W) CMD, the alignment of the main sequence continues almost along the entire MS length.

When using $(A_X/A_V)_{\text{plat}}$, there is a full-isochrone position difference between the FBER isochrone and the fixed-extinction isochrones, as is seen in Figure 3.10. Since all four isochrones with added extinction in this figure assume that $A_V = 1.0$, alignment of the upper main sequences when using $(A_X/A_V)_{\text{plat}}$ is achieved by having a lower value of A_V for the fixed-extinction isochrones than for the function-based case. Depending on the exact value of the fixed A_X/A_V used for fitting a given observed cluster, the

resulting value calculated for A_V and, subsequently, $E(B - V)$ could be significantly underestimated.

3.5 NGC 6793

The final Gaia observational sample of stars in NGC 6793 is shown as a distance-corrected CMD in Figure 3.11, with distances and photometric errors propagated directly from parallax measurements.

Looking at the distances to the objects in the final sample, it is clear that there are significant variations in the observed parallaxes of individual stars, far beyond the maximum cluster radii expected for the largest open clusters, given as 16.8 ± 2.4 pc by Schilbach et al. (2006) or even radii of compact stellar associations, given as 33.2 ± 21.7 pc in the same paper. Some objects in the original dataset (338 members in total) were even assigned negative parallax values, which are physically impossible, as a result of measurement errors. Figure 3.12 shows a histogram of the final NGC 6793 sample. It is clear that a substantial fraction of this sample have measured parallax distances which put them outside the physical limits of better-studied open clusters.

However, the errors in the parallax data for objects assigned to NGC 6793 were significant, as shown in Figure 3.11, particularly for stars in the lower main sequence. This trend is to be expected, since stars in the lower main sequence are the faintest objects in the data and therefore are the most difficult to track against background sources. The significance persists despite this project assuming that the only sources of photometric error are the parallax measurements. This leads to errors in the predicted $M_{\text{ext},X}$ magnitudes, which are calculated by rearranging Equation ??.

Since the table of photometric fluxes did not include photometric errors, the parallax errors alone accounted for the total error in the calculated $M_{\text{ext},X}$. Therefore, the errors on the flux measurements, calculated via error propagation, were fully independent of the absolute magnitude value of a given star. The errors on the $(G_{\text{bp}} - G_{\text{rp}})$ color index were calculated as standard, by adding the individual filter errors in quadrature, giving the color errors which were a factor of $\sqrt{2}$ greater than those for the individual filter fluxes.

Before comparisons with the GC18 parameters can be made, a reference isochrone, with a globally-fixed A_X value of 0.843 and age of 600 Myr (in accordance with Table ??), was made. The A_X/A_V values required to achieve alignment with the upper main sequence were equal to the $(A_X/A_V)_{\text{plat}}$ values for each Gaia filter. While the results from GC18 do not include a metallicity estimate for NGC 6793, it can be estimated from its age that a solar-like metallicity is likely. Therefore, the relevant isochrone has

Cluster property	K05	GC18	This project
Age / Myr	437	603	500
A_V / mag	0.53	0.843	1.1
$[Fe/H]$?	?	0.062
Members	?	271 (photometric)	274

Table 3.3: Comparison of results from this project with observational parameters for NGC 6793 from Table ??

a metallicity of $[Fe/H] = 0$. Due to the overall red-ward shift of the isochrone caused by using $(A_X/A_V)_{plat}$, as demonstrated in Figure 3.10, the GC18 parameter values are not accurate when using model functions to simulate extinction in the isochrones for NGC 6793.

The alignment of the upper main sequence for a FBER treatment was achieved using a value of $A_V = 1.1$. The best-fit MSTO of this isochrone had an age of 500 Myr. To better align the lower main sequence, an increase in isochrone metallicity was required. The best-fit metallicity value was found to be $[Fe/H] = 0.062$. However, the magnitudes of the errorbars (see Figure 3.11) dwarf any isochrone position changes due to changing extinction treatments in the main sequence. The uncertainties also render differences in position between isochrones with similar parameters insignificant, including at the MSTO, as shown in the inset plot in Figure 3.13.

The wide range of distances determined for the individual stars included in the final sample, as mentioned earlier, is orders of magnitude greater than is the case for the largest better-known clusters. Stars whose distances place them furthest from the projected cluster centre make up a significant portion of the objects which are widely scattered from the expected position of the main sequence. Therefore, between this and the magnitude of the errorbars in the lower main sequence in particular, the isochrone fits shown in Figure 3.13 can be considered accurate.

A potential source of uncertainty when comparing the best-fit isochrone results of this project for NGC 6793 with those from GC18 comes from the fact that this project employs the latest BaSTI isochrone database (Hidalgo et al., 2018), while GC18 uses the PARSEC isochrone database (Marigo et al., 2017). The use of different isochrone software could impact the validity of comparing the A_V values, ages and metallicities arising from both extinction treatments.

Gontcharov et al. (2019) carried out a detailed set of observations of the Galactic globular cluster NGC 5904 in 29 photometric bands. The CMDs created from this data were used to fit isochrones from five different databases, including PARSEC and BaSTI. They adopted the Cardelli et al. (1989) extinction law with the parameters

Cluster property	PARSEC	BaSTI
$E(G_{\text{bp}} - G_{\text{rp}}) / \text{mag}$	0.080 ± 0.02	0.013 ± 0.03
Age / Gyr	11.5	12.5
Distance / pc	7600	8400

Table 3.4: Comparison of best-fit parameter results for NGC 5904 using PARSEC and BaSTI. Data taken from Gontcharov et al. (2019).

having values of $R_V = 3.60 \pm 0.05$ and $A_V = 0.20 \pm 0.02$. As shown in Table 3.4, the Gaia colour excess $E(G_{\text{bp}} - G_{\text{rp}})$ for NGC 5904 differs significantly between the best-fits from the two databases, which in turn causes disagreements for the projected cluster age and (photometric) distance. Across all filter systems and isochrone databases, the authors calculated mean estimates of the cluster properties and found that the resulting photometric distance to be in agreement with the cluster distance calculated from the Gaia parallaxes of the cluster members.

In the case of the analysis of NGC 6793 made here, the distance measurements are derived from parallax measurements and so are unaffected by the choice of isochrone software, allowing the GC18 cluster distance to be validly assumed here (as 600 pc to the cluster centre). Furthermore, using the PARSEC-derived parameters from GC18, an accurate BaSTI model isochrone was produced successfully, without any deviation from standard assumptions made for an extinction model with a globally-constant value of A_X/A_V . Therefore, it was concluded that the validity of comparing of the respective A_X , $[\text{Fe}/\text{H}]$ and age values from GC18 and this project was not endangered by the use of different isochrone databases by each study.

As predicted by the comparisons made in Section 3.4.3, the isochrone with a function-based extinction at the GC18 estimated value of $A_V = 0.843$ is systematically too blue and too bright to fit to the observed CMD of NGC 6793. This remains the case regardless of changes in age and metallicity. Therefore, as predicted, there is significant disagreement between the A_V values between the two extinction-calculation methods.

There are considerable uncertainties for the parameters in both isochrones in Figure 3.13. Most fundamentally, the position of the MSTO is reliant only on the position of the four brightest cluster members, of which the brightest two, if the isochrones are accurate, appear to be part of part of the cluster’s SGB hook. The objects’ parallax errors, as shown in the inset of Figure 3.13, are large enough to make any disagreement with either of the isochrones insignificant, even with substantial changes in metallicity. Any changes in A_V and age cause misalignment with the main sequence and MSTO, respectively, making analysis of their impact on the SGB hook region unnecessary.

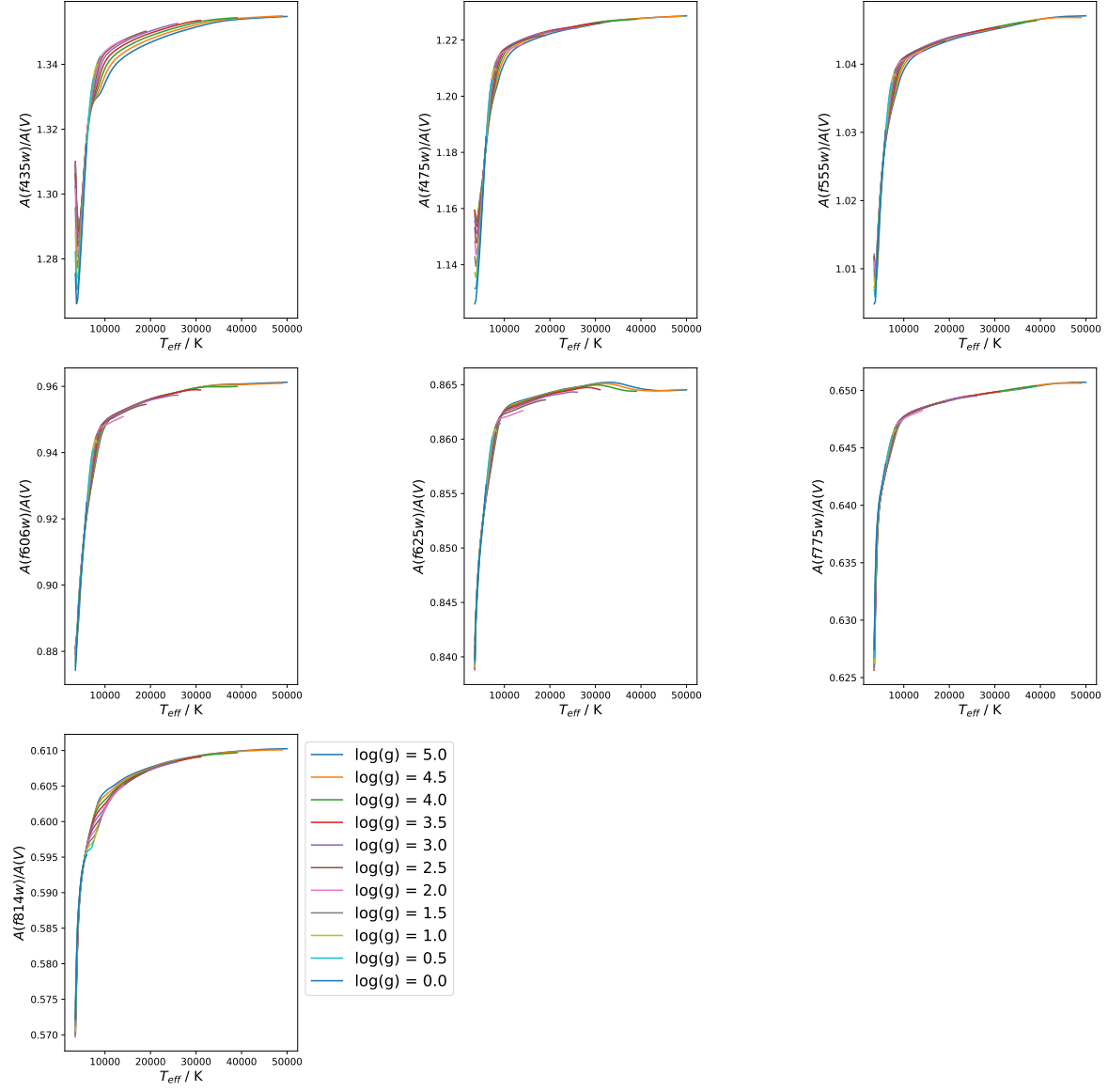


Figure 3.2: Same as Figure 3.1, except the filters shown here are for the ACS system.

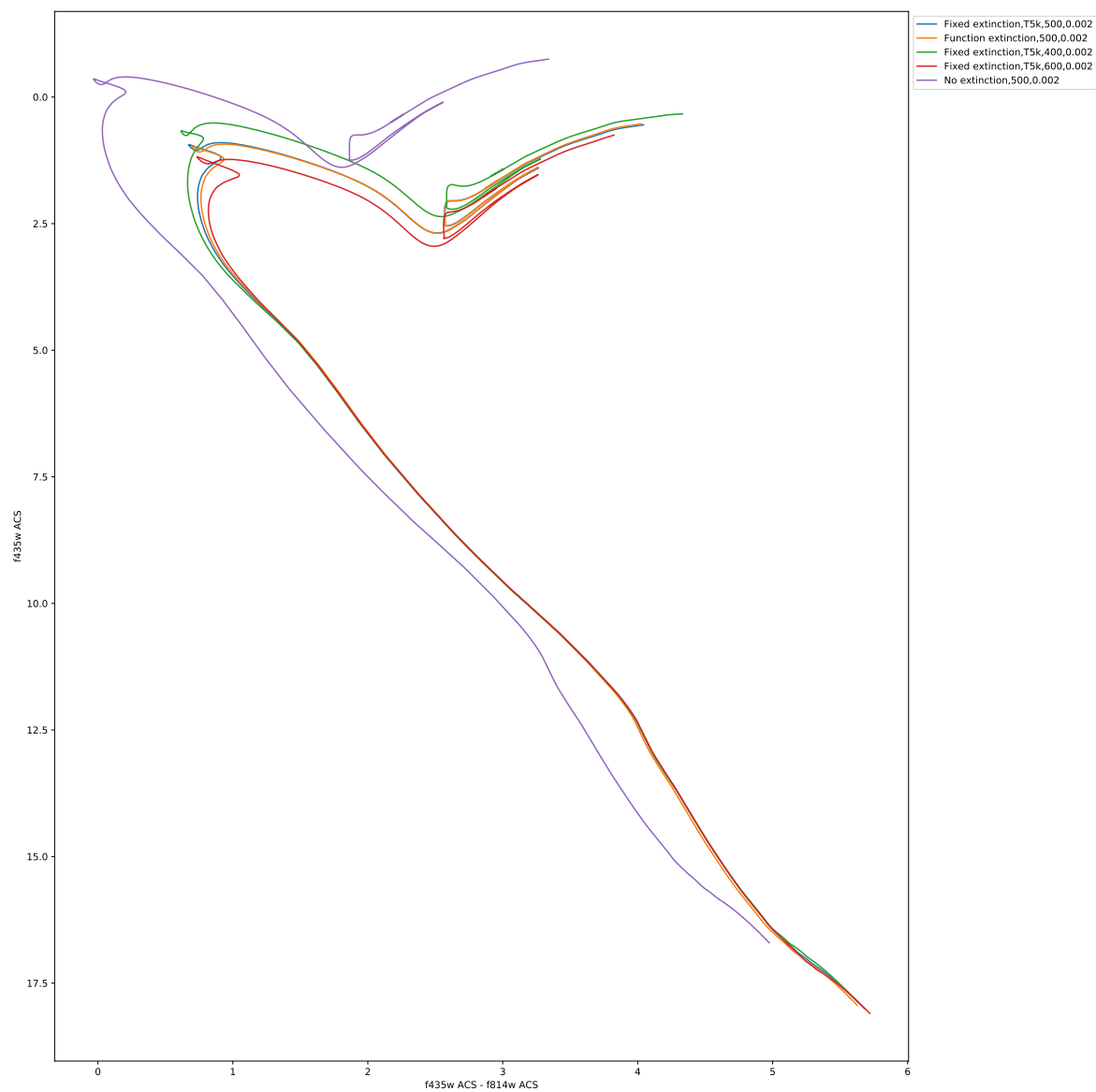


Figure 3.3: ACS F435W-(F435W-F814W) CMD with a fixed extinction ratio equal to $(A_X/A_V)_{MS}$ for each filter

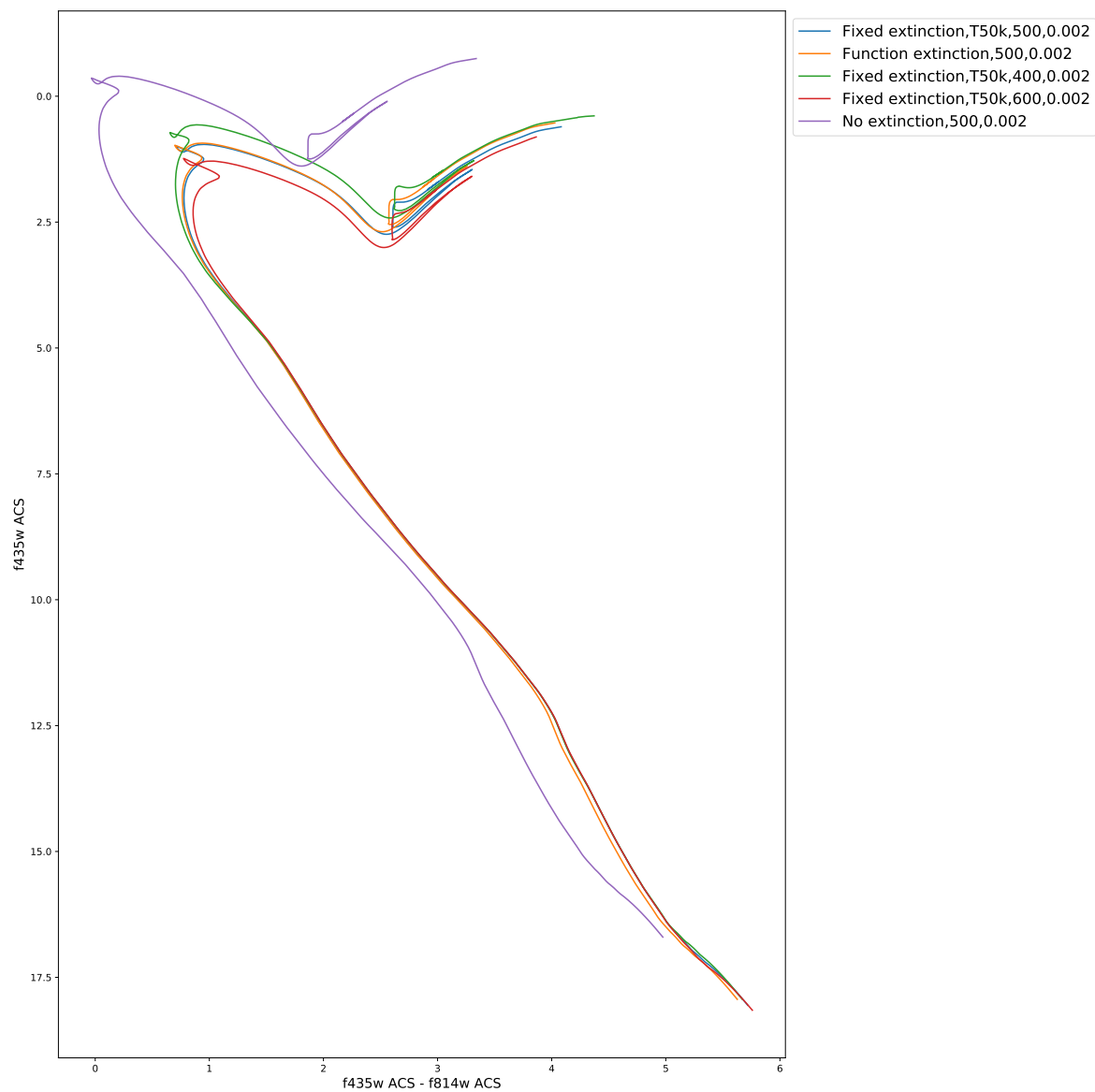


Figure 3.4: ACS F435W-(F435W-F814W) CMD with a fixed extinction ratio equal to $(A_X/A_V)_{plat}$ for each filter

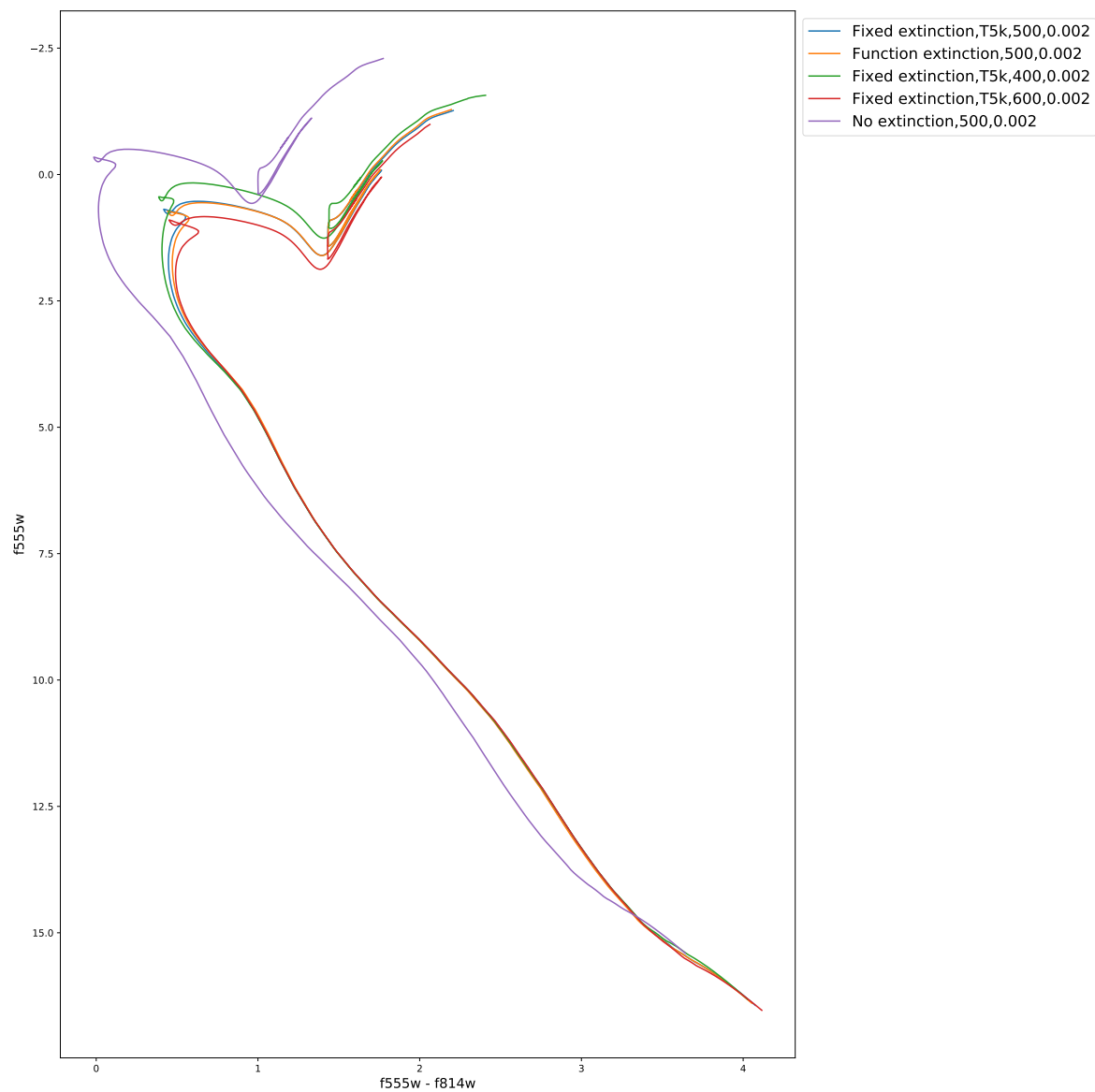


Figure 3.5: WFC3 F555W-(F555W-F814W) CMD with a fixed extinction value equal to $(A_X/A_V)_{MS}$ for each filter

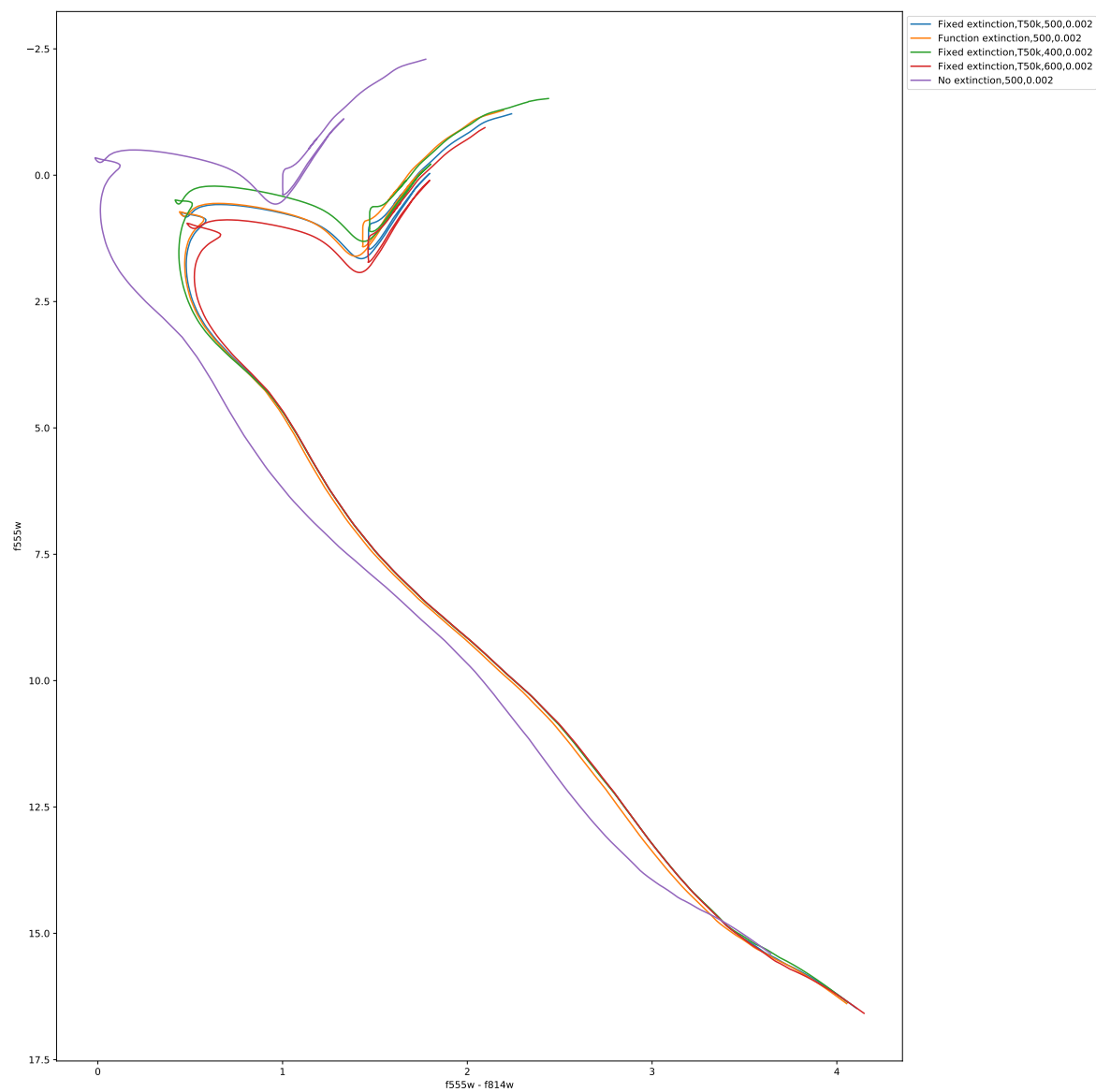


Figure 3.6: WFC3 F555W-(F555W-F814W) CMD with a fixed extinction value equal to $(A_X/A_V)_{plat}$ for each filter

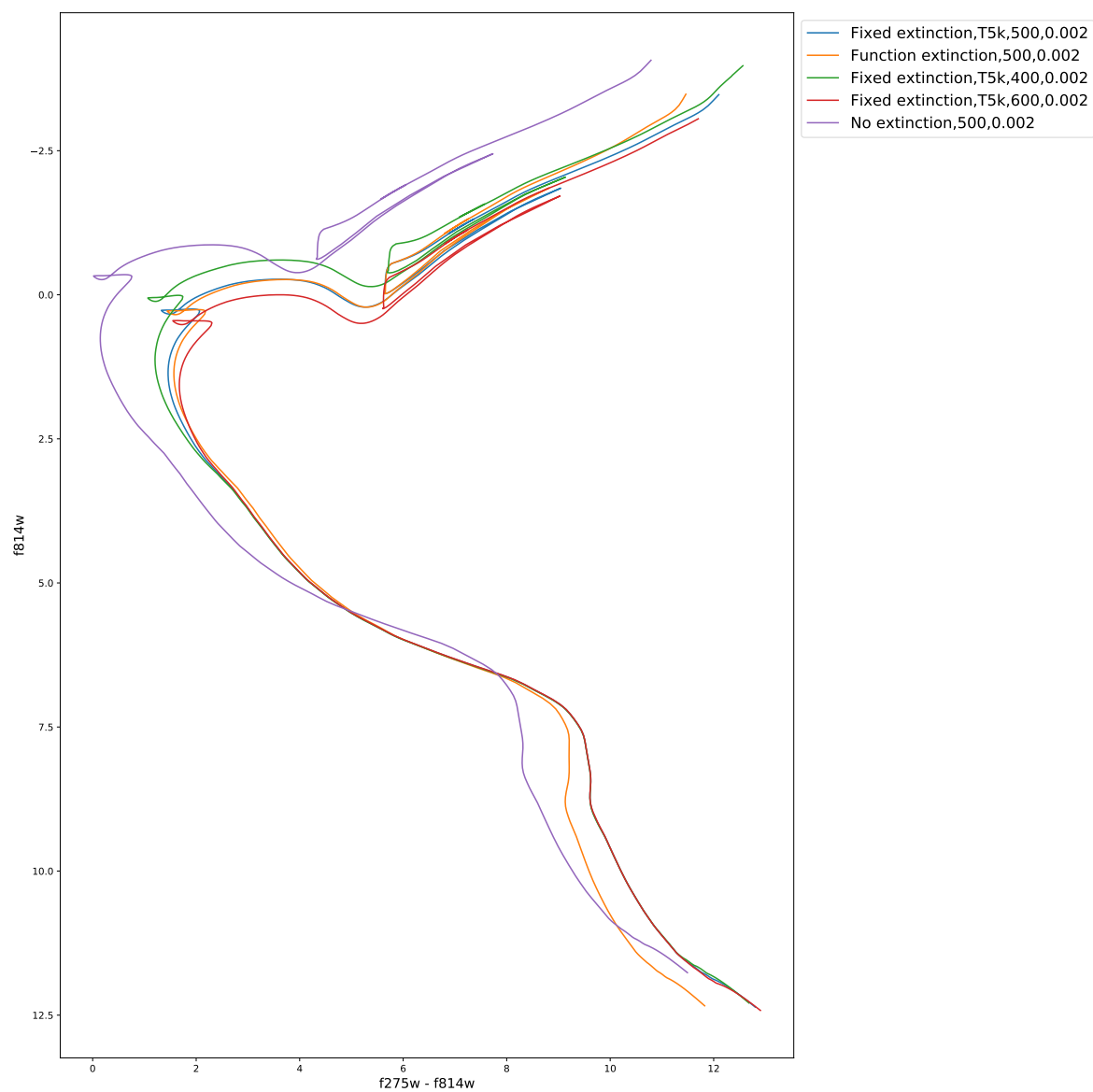


Figure 3.7: WFC3 F814W-(F275W-F814W) CMD with a fixed extinction value equal to $(A_X/A_V)_{MS}$ for each filter.

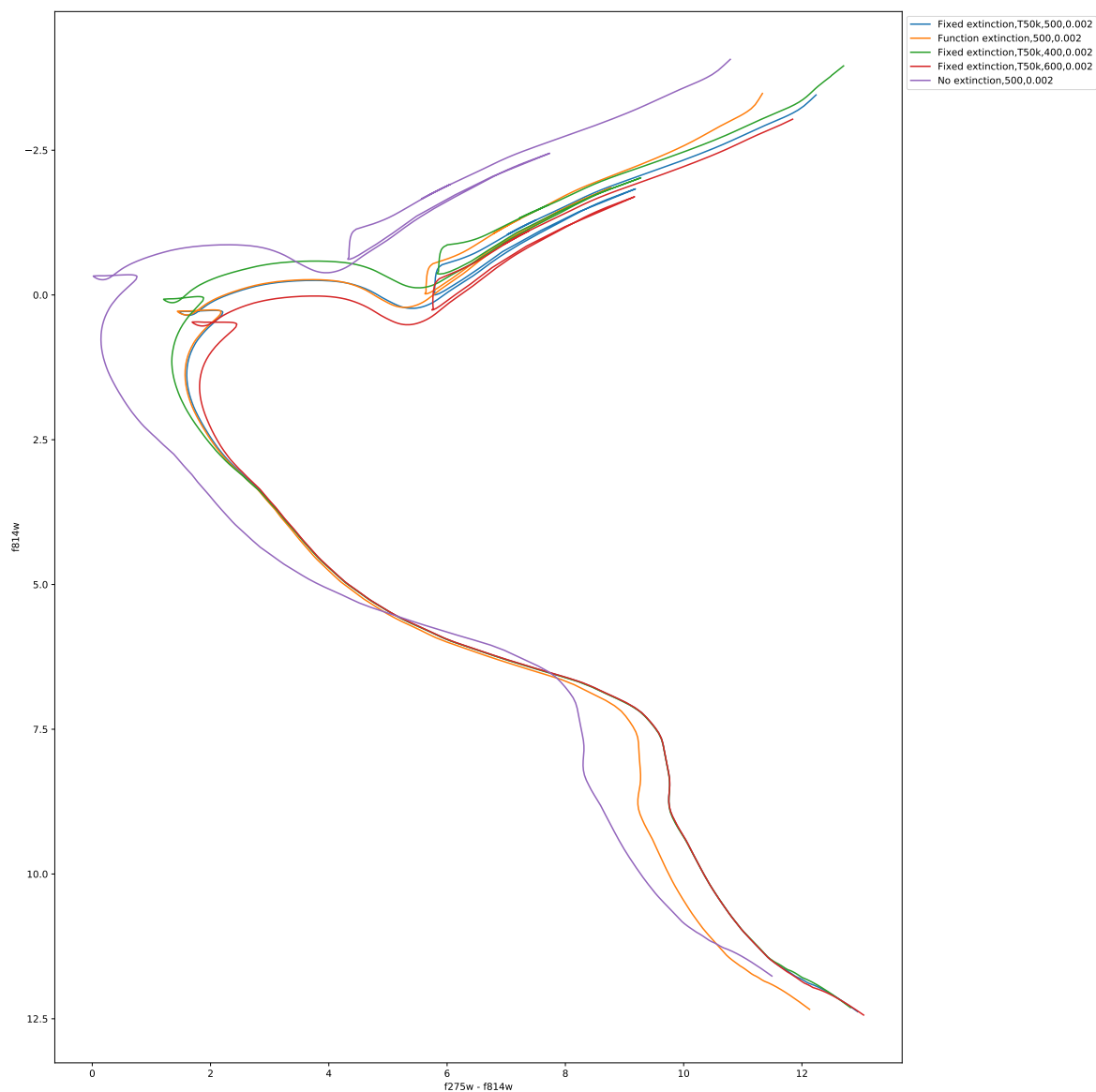


Figure 3.8: WFC3 F814W-(F275W-F814W) CMD with a fixed extinction value equal to $(A_X/A_V)_{plat}$ for each filter

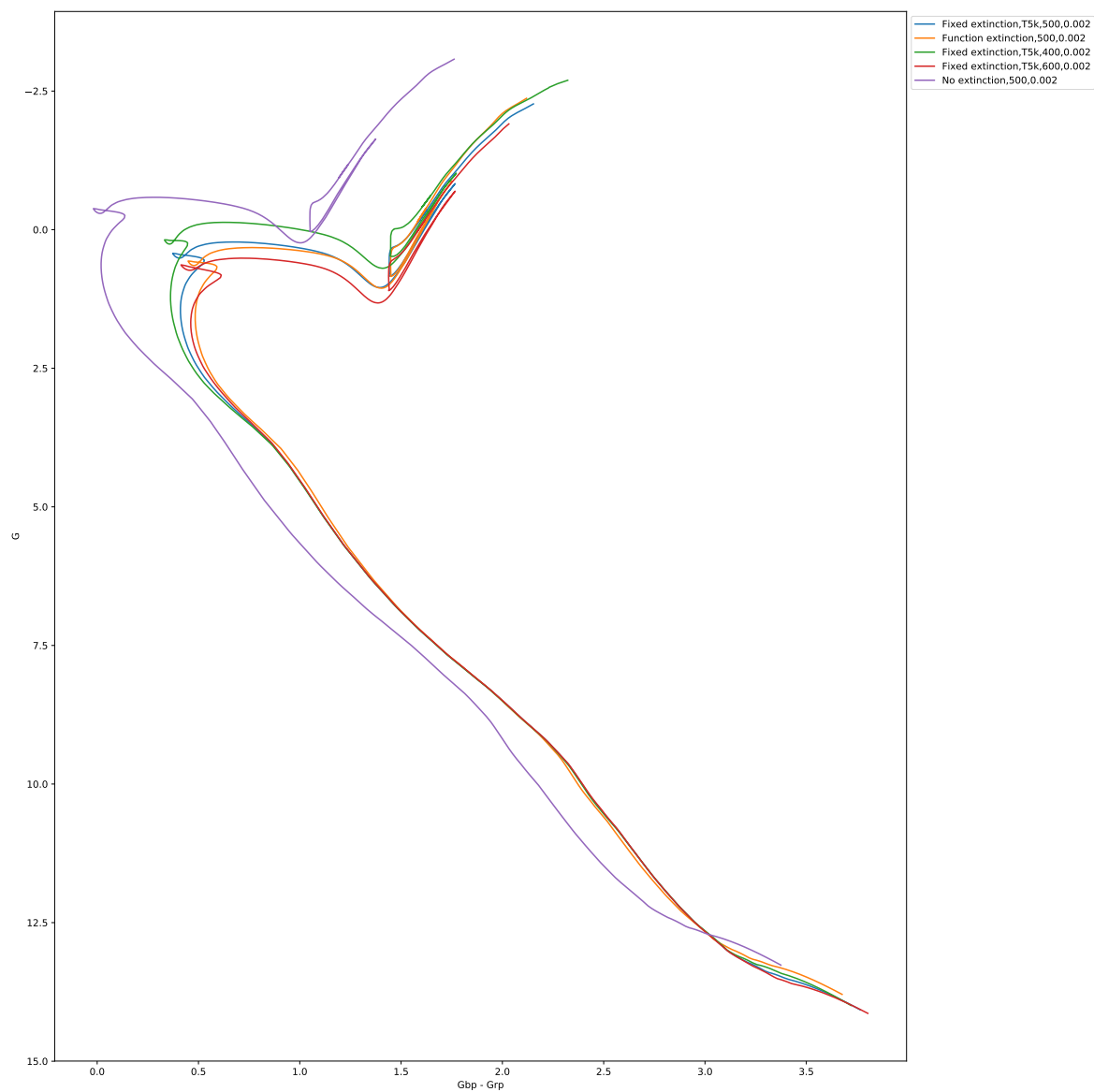


Figure 3.9: Gaia G -(G_{bp} - G_{rp}) CMD with a fixed extinction value equal to $(A_X/A_V)_{MS}$ for each filter

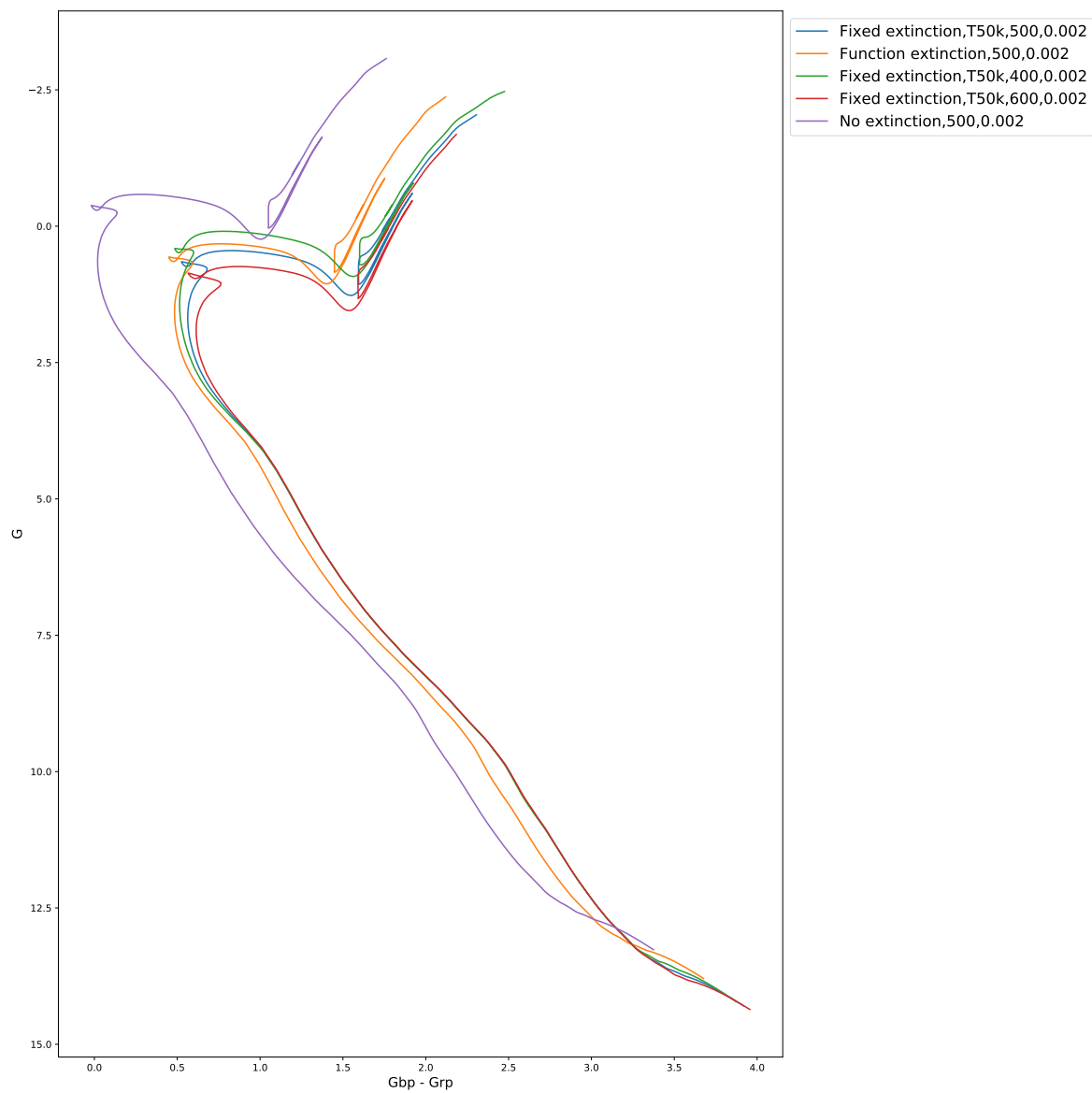


Figure 3.10: Gaia G -(G_{bp} - G_{rp}) CMD with a fixed extinction value equal to $(A_X/A_V)_{plat}$ for each filter

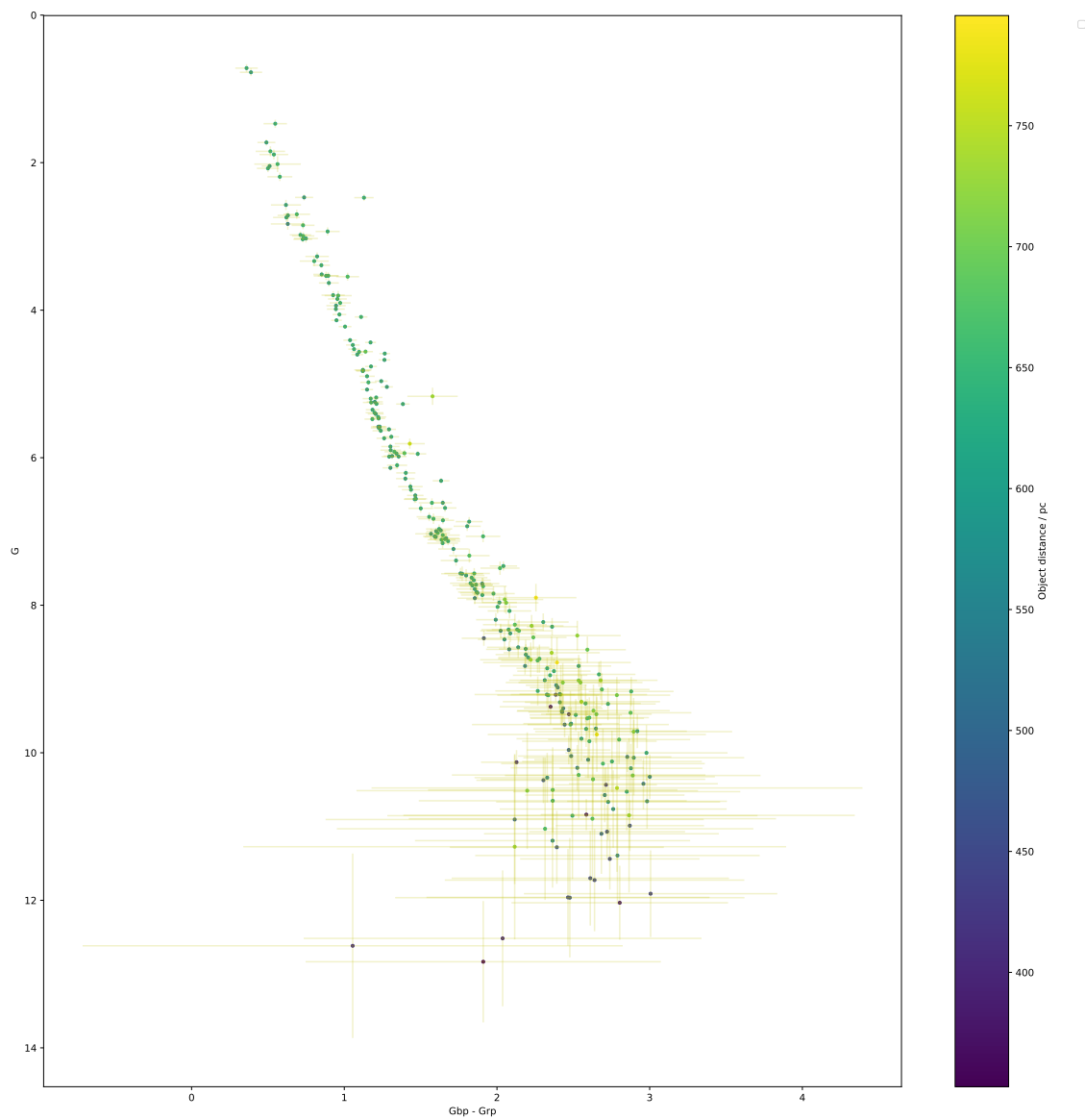


Figure 3.11: Gaia G -(G_{bp} - G_{rp}) CMD showing the 274 cluster members in the final dataset, with errorbars added. The color of each object is determined by its parallax-derived distance.

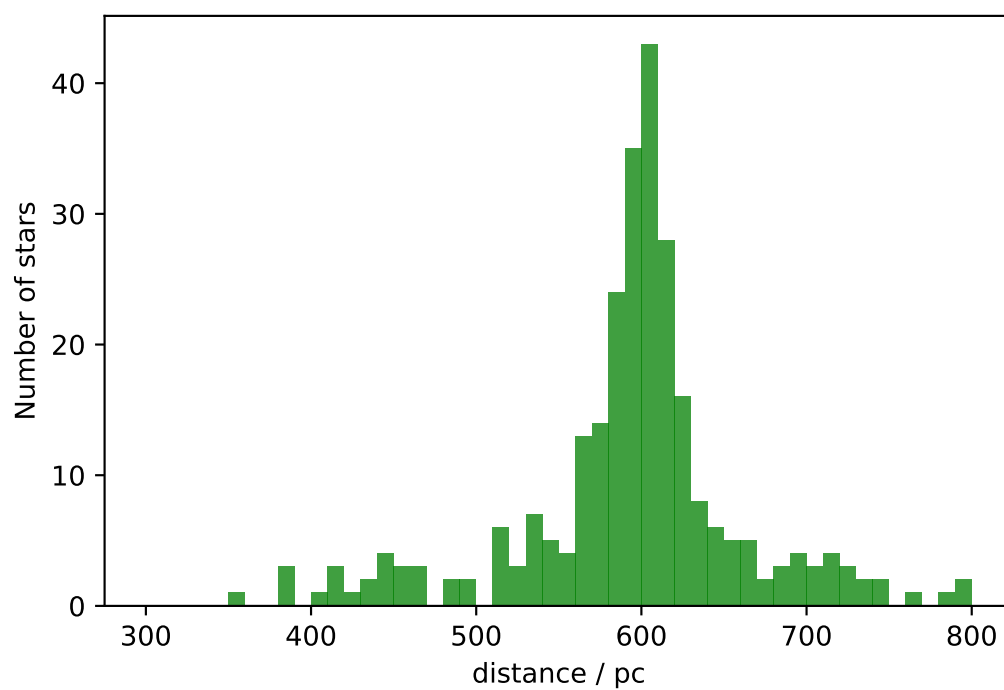


Figure 3.12: Histogram of distances for the 274 stars in the final observational dataset. The bins are set to a fixed width of 10 pc.

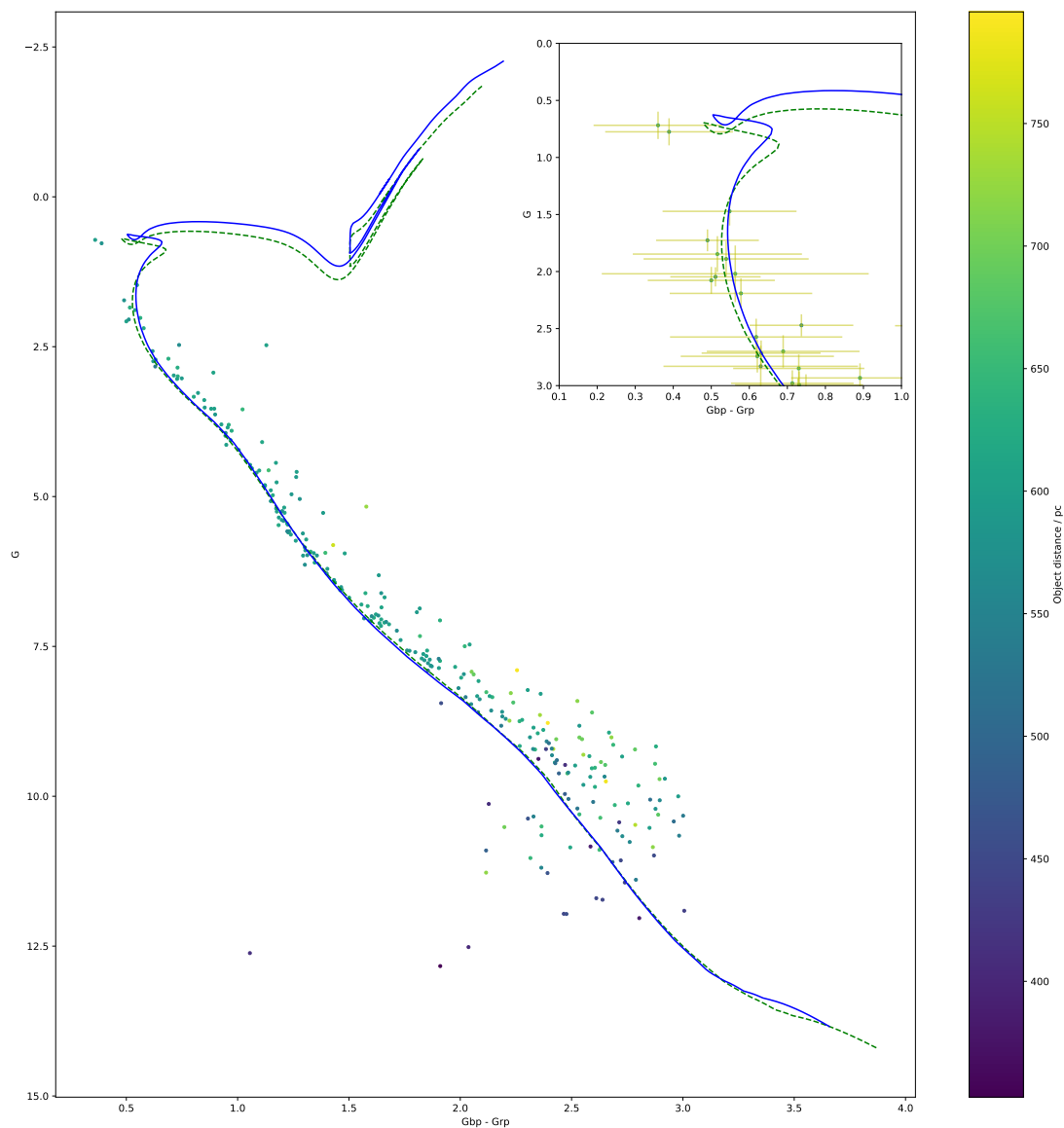


Figure 3.13: Gaia G -(G_{bp} - G_{rp}) CMD showing the 274 cluster members in the final dataset, corrected for their individual distances with errorbars shown. The color of each object is determined by its parallax-derived distance.

Chapter 4

Conclusion & future work

In all cases, applying a fixed extinction to all points in an isochrone causes the main-sequence turn-off to occur at a more luminous, bluer point in a given CMD than the MSTO point for an isochrone with extinction values for every star described using a function fitted to empirically-derived data for each filter.

The significance of this position change is dependent on the filters used to construct the particular CMD in question. The position changes in two of the four CMDs studied are insignificant.

The WFC3 F814W-(F275W-F814W) CMD shows significant differences between the positions of certain sections isochrones treated under different extinction-calculation approaches, particularly for the lower main sequence but also affecting for the MSTO, depending on the value of A_X used in the fixed-extinction case. This is a consequence of the much larger variation of extinction between different stellar types at shorter wavelengths, in this case in the UV.

The Gaia photometric CMD is highly sensitive to the A_X values applied to the filters. This applies not only when comparing the fixed- A_X/A_V approach to the function approach, but also when comparing the fixed approaches using $(A_X/A_V)_{plat}$ and $(A_X/A_V)_{MS}$. This underscores the substantial risk of incorrect assumptions being made when fitting isochrones to observational data with a single globally-fixed A_X value across all stellar models, which in turn leads to incorrect estimates of important cluster parameters.

4.1 Future work

There are multiple ways to extend the applicability of the work done in this project. The most obvious example is both to study more CMDs in the filter systems used in this project acquire and to utilise the response functions of more filter systems, particularly for more modern and more sensitive instruments, such as the James Webb

Space Telescope (JWST) and the proposed WFIRST and PLATO space telescopes, to create extinction-ratio models for observations made with these instruments.

Another extension would be to apply the FBER approach to observed clusters with isochrone ages determined using the globally-fixed A_X approach. If, as predicted for the limited examples studied in this project, the isochrone ages of a given cluster CMD are greater when employing a fixed-extinction approach, there is the possibility of a systematic decrease in the predicted ages of these observed after comparison with ages derived using a function-based approach.

Regarding the case of NGC 6793, follow-up observations with Johnson-Cousins filters, if feasible, could resolve the A_V disagreement between extinction-calculation methods by providing a direct measured value upon which the Gaia extinction ratios can be calculated.

Finally, the limits on the accuracy of the model functions presented here require investigation, particularly the accuracy limit at the lowest T_{eff} values available from ATLAS9. This could be done using the same approach as that used by Girardi et al. (2008), who use models from other sources to extend their bolometric correction database to a minimum T_{eff} of 1000 K. The coolest known stellar objects (excluding brown dwarfs) have $T_{\text{eff}} \gtrsim 2500$ K. Extending the dataset would constrain the allowed behaviour of the model functions in the lowest ATLAS9 metallicities. Currently, the lack of data below 3500 K prevents investigation of the significance of the tail-flick phenomenon, since the phenomenon, at present, extends to (and possibly beyond) the lower- T_{eff} limit for the affected filters.

Bibliography

- Bessell M. S., 1990, *PASP*, 102, 1181
- Cardelli J. A., Clayton G. C., Mathis J. S., 1989, *ApJ*, 345, 245
- Casagrande L., VandenBerg D. A., 2014, *MNRAS*, 444, 392
- Casagrande L., VandenBerg D. A., 2018, *MNRAS*, 479, L102
- Castelli F., Kurucz R. L., 2004, *ArXiv Astrophysics e-prints*
- Fitzpatrick E. L., 1999, *PASP*, 111, 63
- Forbes J. D., 1842, *Philosophical Transactions of the Royal Society of London Series I*, 132, 225
- Gaia Collaboration et al., 2018, *A&A*, 616, A10
- Girardi L., Bertelli G., Bressan A., Chiosi C., Groenewegen M. A. T., Marigo P., Salasnich B., Weiss A., 2002, *A&A*, 391, 195
- Girardi L., et al., 2008, *PASP*, 120, 583
- Gontcharov G. A., Mosenkov A. V., Khovritchev M. Y., 2019, *MNRAS*, 483, 4949
- Grebel E. K., Roberts W. J., 1995, *A&A Suppl. Ser.*, 109, 293
- Gustafsson B., Edvardsson B., Eriksson K., Jørgensen U. G., Nordlund Å., Plez B., 2008, *A&A*, 486, 951
- Hidalgo S. L., et al., 2018, *ApJ*, 856, 125
- Johnson H. L., Morgan W. W., 1953, *ApJ*, 117, 313
- Jordi C., et al., 2010, *A&A*, 523, A48
- Kalirai J. S., Baggett S., Borders T., Rajan A., 2010, Technical report, The Photometric Performance of WFC3/UVIS: Temporal Stability Through Year 1
- Kharchenko N. V., Piskunov A. E., Röser S., Schilbach E., Scholz R.-D., 2005, *A&A*, 438, 1163

- Kharchenko N. V., Piskunov A. E., Schilbach E., Röser S., Scholz R. D., 2013, *A&A*, 558, A53
- Kurucz R., 1993, *ATLAS9 Stellar Atmosphere Programs and 2 km/s grid*. Kurucz CD-ROM No. 13. Cambridge, Mass.: Smithsonian Astrophysical Observatory, 1993., 13
- Lagioia E. P., et al., 2018, *MNRAS*, 475, 4088
- Landgraf M., Krüger H., Altobelli N., Grün E., 2003, *Journal of Geophysical Research (Space Physics)*, 108, 8030
- MacKenty J. W., Kimble R. A., O’Connell R. W., Townsend J. A., 2010, in *Space Telescopes and Instrumentation 2010: Optical, Infrared, and Millimeter Wave*. p. 77310Z
- Marigo P., et al., 2017, *ApJ*, 835, 77
- Mie G., 1908, *Annalen der Physik*, 330, 377
- O’Donnell J. E., 1994, *ApJ*, 422, 158
- Ohvri H., Okulov O., Teral H., Teral K., 1999, *Solar Energy*, 66, 305
- Ortolani S., Cassisi S., Salaris M., 2017, *Galaxies*, 5, 28
- Pietrinferni A., Cassisi S., Salaris M., Castelli F., 2004, *ApJ*, 612, 168
- Pols O. R., Schröder K.-P., Hurley J. R., Tout C. A., Eggleton P. P., 1998, *MNRAS*, 298, 525
- Rieke G. H., Lebofsky M. J., 1985, *ApJ*, 288, 618
- Sahu K., Deustua S., Sabbi E., 2014, Technical report, *WFC3/UVIS Photometric Transformations*
- Sarajedini A., et al., 2007, *ApJ*, 133, 1658
- Schilbach E., Kharchenko N. V., Piskunov A. E., Röser S., Scholz R.-D., 2006, *A&A*, 456, 523
- Sirianni M., et al., 2005, *PASP*, 117, 1049
- Valencic L. A., Clayton G. C., Gordon K. D., 2004, *ApJ*, 616, 912
- Witt A. N., 2000, *Journal of Geophysical Research (Space Physics)*, 105, 10299